A new methodology to train fracture network simulation using Multiple Point Statistics

Pierre-Olivier BRUNA[(1)*], Julien STRAUBHAAR[(2)], Rahul PRABHAKARAN[(1, 3)], Giovanni BERTOTTI[(1)], Kevin BISDOM[(4)], Grégoire MARIETHOZ[(5)], Marco MEDA[(6)].

(1) Department of Geoscience and Engineering, Delft University of Technology, Delft, the Netherlands.
(2) Centre d'hydrogéologie et de géothermie (CHYN), Université de Neuchâtel, Emile-Argand 11, CH-2000 Neuchâtel.
(3) Department of Mechanical Engineering, Section of Energy Technology, Eindhoven University of Technology, Eindhoven the Netherlands.
(4) Shell Global Solutions International B.V., Grasweg 31, 1031HW Amsterdam, The Netherlands
(5) University of Lausanne, Institute of Earth Surface Dynamics (IDYST) UNIL-Mouline, Geopolis, office 3337, 1015 Lausanne, Switzerland
(6) ENI Spa, Upstream and Technical Services, San Donato Milanese, Italy.

* Corresponding author, p.b.r.bruna@tudelft.nl

Abstract

Natural fracture network characteristics can be known from high-resolution outcrop images acquired from drone and photogrammetry. These outcrops might also be good analogues of subsurface naturally fractured reservoirs and can be used to make predictions of the fracture geometry and efficiency at depth. However, even when supplementing fractured reservoir models with outcrop data, gaps in that model will remain and fracture network extrapolation methods are required. In this paper we used fracture networks interpreted in two outcrops from the Apodi area in Brazil to present a revised and innovative method of fracture network geometry prediction using the Multiple Point Statistics (MPS) method.

30   The MPS method presented in this article uses a series of small synthetic training images

31   (TIs) representing the geological variability of fracture parameters observed locally in the

32   field. The TIs contain the statistical characteristics of the network (i.e. orientation, spacing,

33   length/height and topology) and allow representing complex arrangement of fracture

34   networks. These images are flexible as they can be simply sketched by the user.

35   We proposed to use simultaneously a set of training images in specific elementary zones of

36   the Apodi outcrops defined in a probability map in order to best replicate the non-stationarity

37   of the reference network. A sensitivity analysis was conducted to emphasize the influence of

38   the conditioning data, the simulation parameters and the used training images. Fracture

39   density computations were performed on the best realisations and compared to the reference

40   outcrop fracture interpretation to qualitatively evaluate the accuracy of our simulations. The

41   method proposed here is adaptable in terms of training images and probability map to ensure

42   the geological complexity is accounted for in the simulation process. It can be used on any

43   type of rock containing natural fractures in any kind of tectonic context. This workflow can

44   also be applied to the subsurface to predict the fracture arrangement and fluid flow efficiency

45   in water, heat or hydrocarbon fractured reservoirs.

46

I] Introduction

I.1 The importance of the prediction of fracture network geometry

49   Fracture are widespread in Nature and depending on their density and their aperture, they

50   might have a strong impact on fluid flow and fluid storage in water (Berkowitz, 2002;

51   Rzonca, 2008), heat (Montanari et al., 2017; Wang et al., 2016) and hydrocarbon reservoirs

52   (Agar and Geiger, 2015; Lamarche et al., 2017; Solano et al., 2010) They are typically

53   organised as networks ranging from nanometre to multi-kilometre scale (Zhang, 2016), and

54   present systematic geometrical characteristics (i.e. type, orientation, size, chronology,

55 topology) that are determined from specific stress and strain conditions. These conditions

56 have been used to derive concepts of fracture arrangements in various tectonic contexts and

57 introduced the notion of geological fracture-drivers (fault, fold, burial, facies). Based on these

58 drivers it is possible to some extent to predict reservoir heterogeneity and to define potential

59 permeability pathways within the rock mass (Lamarche et al., 2017; Laubach et al., 2018).

60 Despite the existence of these concepts, a range of parameters including fracture abutment

61 relationships as well as height/length distributions cannot be adequately sampled along a 1D

62 borehole and are mainly invisible on seismic images. In addition, fracture networks may

63 present a spatial complexity (variability of orientation or clustering effect) that is also largely

64 unknown in the subsurface. Long and Witherspoon, (1985) and Olson et al., (2009) showed

65 how those parameters impact the connectivity of the network and consequently affect fluid

66 flow in the subsurface. In outcrops, the fracture network characteristics can be observed and

67 understood directly. Consequently, outcrops are essential to characterize fracture network

68 attributes that cannot be sampled in the subsurface, such as length or spatial connectivity.

69

70 **I.2 Surface rocks as multiscale reservoir analogues**

71 In this context, the study of outcrop analogues is one of the few ways to constrain the

72 architecture of fracture networks (Bisdom et al., 2014; Bruna et al., 2017; National Research

73 Council, 1996; Lamarche et al., 2012; Lavenu et al., 2013). Outcrops can be considered as a

74 natural laboratory where the structural reality can be observed and quantified at various

75 scales. At the small – measurement station – scale (order of 10's m), fracture type,

76 chronologies and topology relationships can be characterised using classical ground-based

77 structural geology method such as scanlines (Lavenu et al., 2013; Mauldon et al., 2001). At

78 the intermediate – outcrop – scale (order of 10^2's m), length of fractures and geometry

79 variability can be qualified and quantified using unmanned aerial vehicles (UAV - drones).

80   Working on outcrops allows an understanding of the geological history of the targeted area

81   and eventually to decipher how, when and where fractures were developed. In addition,

82   outcrops constitute an efficient experimental laboratory where some of properties of the

83   fracture network (i.e. fracture distribution, apertures, permeability and fluid flow behaviour)

84   can be known and modelled (Bisdom et al., 2017). At the large – reservoir – scale (order of

85   10^{3-4}m) satellite imagery and geophysical maps provide the characterisation of the 100's of

86   meter long objects such as large fracture systems or faults.

87   However, not every outcrop can be considered as a good analogue for the subsurface. Li et al.,

88   (2018), in their work on the Upper Cretaceous Frontier Formation reservoir, USA, observed

89   significant differences in the fracture network arrangement in subsurface cores compared to

90   an apparent good surface analogue of the studied reservoir. In the subsurface, fractures

91   appeared more clustered than in the outcrop where the arrangement is undistinguishable from

92   random. The origin of these differences is still debated but these authors suggest that

93   alteration (diagenesis) or local change in pressure-temperature conditions, may have

94   contributed to the observed variability. The near-surface alteration processes (exhumation,

95   weathering) may also ontributed to misinterpretations of the characteristics of the network. In

96   this case, one should be particularly careful while using observed networks to make geometry

97   or efficiency (porosity, permeability) predictions in the subsurface. Therefore, the application

98   to the subsurface of the characteristics observed in the outcrop is not always straightforward

99   or even possible, and may lead to erroneous interpretations. Relatively unbiased signals such

100   as stylolites or veins and particular geometric patterns might be a trustful basis to show that

101   the studied outcrop can be, to some extent, compared to the subsurface.

102

103   **I.3 Modelling approaches classically used to model fracture network geometries**

The widely used discrete fracture network (DFN) stochastic modelling tools provide statistical representation of fracture networks constrained generally by univariate and random distribution of orientation, size, spacing and density/intensity data (Bisdom et al., 2014; Bisdom et al., 2017; Huang et al., 2017; Panza et al., 2018). The generated models follow a local stationarity hypothesis. This implies that the statistics used during the simulation are constant in the defined area of interest (Deutsch and Journel, 1997; Gringarten and Deutsch, 1999; Gringarten and Deutsch, 2001; Journel and Zhang, 2006). Liu et al., (2009), highlighted the implicit randomisation that conventional DFN models produce and demonstrated that parameters like fracture connectivity are poorly considered in these representations. In addition, it is generally admitted that discrete realisations of thousands of fractures objects at the kilometre scale are computationally very demanding and often even impossible (Jung et al., 2013). Some authors attempted to use a pixel-based method to try to predict fracture network geometries. Bruna et al., (2015), used a dense hydrogeological borehole survey sampling a Lower Cretaceous aquifer in the SE of France to define fracture facies and to model their distribution with two-points geostatistics. In this case, the amount of available data and their consistency helped to provide realistic results. However, far from conditioning data (i.e. boreholes) the fractures simulation are poorly constrained.

The work of Hanke et al., (2018) uses a directional semi-variogram to quantify fracture intensity variability and intersection density. This contribution provides an interesting way to evaluate the outputs of classical DFN approaches but requires a large quantity of input data that are not always available in the subsurface. To geologically represent the fracture network geometry in various contexts, an alternative method has to be developed. This innovative method needs to i) explicitly predicts the organisation and the characteristics of multiscale fracture objects, ii) takes into consideration the spatial variability of the network and iii) requires a limited amount of data to be realised.

129

I.4 Multi-point statistics as an alternative to classic DFN approaches

Since Liu et al., (2002), few authors highlighted the potential of using multi-point statistics

(MPS) to generate realistic fracture networks (Chugunova et al., 2017; Karimpouli et al.,

2017). Strebelle, (2002) showed how the MPS are able to reproduce any type of geological

heterogeneities of any shape at any size as long as they present a repetitive character. This

characteristic seems particularly well adapted to predict the geometry of a fracture network.

The MPS method uses training images (TI) to integrate conceptual geological knowledge into

geostatistical simulations (Mariethoz, 2009). The TI is a grid containing geological patterns

that are representative of a certain type of geological structure, type and arrangement. The TI

can be considered as a synthetic model of the geological heterogeneity (i.e. all the elements

characterising a geological object) likely to occur in a larger domain (i.e. reservoir, aquifer,

outcrop). The TI must include the possible range and shape of the geobodies that the

geoscientist intends to model, as well as the relationship these geobodies have with each other

(Mariethoz, 2009; Strebelle, 2002).

144

I.5 Objectives and contents of this research

In this paper we propose a MPS workflow considering the geological variability of the

fracture network geometry in outcrops (size order of 100m) and a methodology on how to use

this method at the reservoir scale. The approach is based on the direct sampling method

(Mariethoz et al., 2010) and uses multiple training images for a single realisation (Wu et al.,

2008). The concept of the probability map has been revised here to define where a training

image should be used in the simulation grid. Our outcrop-based simulations also take into

account "seismic-scale" objects (i.e. object longer than 40m) considered as hard conditioning

data. The proposed workflow is tested on outcrops considered as analogues of the Potiguar

154 Basin, Brazil where fracture network have been previously characterised and interpreted from

155 drone imagery (Bertotti et al., 2017; Bisdom, 2016). Uncertainties were evaluated by

156 comparing original outcrop interpretation (done manually by a geologist) with the geometrical

157 characteristics of the network generated from MPS. To evaluate the quality of the simulations,

158 we computed density maps in outcrop fracture interpretation and on selected stochastic

159 models. The proposed approach is innovative and provides a quick and efficient way to

160 represent fracture network arrangements at various scales.

161

II] Methodology

II.1 The direct sampling method

164 The direct sampling method (DS) was introduced by (Mariethoz et al., 2010). Figure 1,

165 synthesizes the DS modelling process developed thereafter. The method requires a simulation

166 grid where each node is initially unknown and called x, a training image grid (TI) where each

167 node is known and called y i.e. V(y) is defined where V is the variable of interest (e.g. facies

168 value). The simulation proceeds as follows. First, the set of conditioning data (if present) is

169 integrated in the simulation grid. Then, each remaining unknown node x is visited following a

170 random or defined path, and simulated as follows. 1) The pattern $d_n(x) =$

171 $(x_1, V(x_1)),...,(x_n, V(x_n))$ formed by the at most **n** informed nodes the closest to x is retrieved.

172 Any neighbour x_i of x is either a previously simulated node or comes from the conditioning

173 data set. The lag vectors $h_i = x_i - x$ define the geometry of the neighbourhood of x. The

174 combination of the value and position of x_i defines the data event or pattern $d_n(x)$. 2) Then, the

175 TI is randomly scanned to search for a pattern $d_n(y)$ similar to $d_n(x)$. For each scan node y, the

176 pattern $d_n(y) = (y_1, V(y_1)),...,(y_n, V(y_n))$, where $y_i = y + h_i$, is compared to $d_n(x)$ using a distance

177 (Meerschman et al., 2013). When the distance is lower than an acceptance threshold (t)

178 defined by the user or if the proportion of scanned nodes in the TI reaches a maximal fraction

179 (**f**) defined by the user, the scan is stopped and the value of the best candidate **y** (pattern with

180 the minimal distance) is directly attributed to **x** in the simulation grid (i.e. *V(x)* = *V(y)*).

181 As the DS method does not use a catalogue of all possible patterns found in the TI, it is

182 extremely flexible and in particular allows taking into account both categorical and

183 continuous variables and managing multivariate cases, provided that the pattern distance is

184 suitable. In this paper we are using the DeeSse version of the direct sampling code

185 (Straubhaar, 2017).

186

187 **II.2 Multiscale fracture attributes**

188 To evaluate how the direct sampling method is dealing with the fracture network, the present

189 experimentation is based on outcrop data where the present-day "structural reality" is

190 observable at various scales. Pavements (i.e. horizontal surfaces in the order of 10^2 m scale)

191 were targeted because these objects contain important information that is not always

192 accessible with standard vertical outcrops (Corradetti et al., 2017a; Corradetti et al., 2017b;

193 Tavani et al., 2016) or with classic geophysical imagery. Pavement sizes allow the user to

194 interpret and localise fracture patterns variability (Bruna et al., 2018). For instance, clusters of

195 fractures (i.e. local increase of the fracture density) can be identified by the interpreter.

196 Pavements also allow to obtain quantitative data on fracture lengths, which are usually

197 difficult to get in vertical cliff. In the subsurface, data can be provided by geophysical 3D

198 maps and fracture attribute detection tools (Chopra and Marfurt, 2007; Somasundaram et al.,

199 2017). However, these tools are not always available and detect the longer lineaments only.

200 Working with pavements constitutes an asset as small-scale investigation can be conducted in

201 key zones of the outcrop (i.e. in folded areas, each compartment or dip domain of the fold

202 should be imaged and investigated in detail) where the gathered data will help to calibrate

203 larger scale information. Classical fieldwork methods (observation and characterisation,

204 measurements, statistical analyses, sampling) help interpreting fracture families and are

205 essential to constrain larger scale observation.

206 In this study, UAV-based photogrammetry is used to obtain an orthorectified mosaic and 3D

207 digital outcrops models (Bemis et al., 2014; Claes et al., 2017; Vollgger and Cruden, 2016).

208 The scale of these images is an intermediate between the scale of measurement station and

209 that of satellite imagery. Digitization of fracture traces, geological contacts, sedimentary

210 structures and structural domain boundaries are currently processed by hand and represent a

211 considerable time investment. In this contribution, fractures were interpreted in orthomosaic

212 images with the help of GIS software. Length, azimuth, fracture family proportions and

213 fracture density statistics were extracted from the interpretation. In addition, a series of

214 measurement station (area of about 2×2 m) information was acquired and compared with the

215 dataset from the drone imagery in order to align interpretations and provide coherent fracture

216 history.

217

218 **II.3 Training images, conditioning data and probability maps**

219 • **Training images**

220 Training images (TI) are the base input data of the MPS simulation. Building them is a critical

221 step to succeed a realisation (Liu et al., 2009). The TI is a pixelated image based on a local

222 interpretation of a geological phenomenon (i.e. an interpreted photography taken from a local

223 zone of interest in the field) or digitised by a geologist and based on geological concepts

224 (Strebelle, 2002). These images should synthesise all of the recognized geological parameters

225 that characterise the area to simulate. This implicitly means that the proportion of facies

226 carried by the TI, will be reproduced into the simulation grid but this also requires extensive

227 pre-processing work (see example of TIs in figures 5, 6, 9 and 10). To manage this

228 complexity, we used multiple training images where facies proportion and geometrical

229   distribution can vary. Hence, each TI has a local impact on the simulation. Moreover, in our

230   approach fractures sets are grouped in facies in the TI, based primarily on their orientation

231   and possibly on their length or additional parameters defined by the user. The fractures

232   classification helps reproducing patterns and simplifies the process of building the TI.

233   • **Conditioning data**

234   One limitation of the MPS methods is the tendency to disconnect long continuous objects (i.e.

235   typically fractures, (Bruna et al., 2017). To manage this issue, long fractures can be identified

236   and incorporated into the simulation as conditioning data. As per the training images, such

237   data can be integrated as pixelated grids. They may come from satellite imagery or they can

238   be interpreted from gravity or magnetic surveys or from 3D seismic imagery (Magistroni et

239   al., 2014).

240   • **Probability map**

241   The direct sampling method can be used with multiple training images. In this situation, the

242   user provides a set of TIs, and for each TI a probability map defined on the simulation grid,

243   giving at each node the probability to use that TI. The pixel-wise sum of these maps should

244   then be equal to one in every node. If each TI corresponds to a partition of the area of interest,

245   with for each TI one elementary zone, covering the whole simulation grid, the probabilities in

246   the map are set to one for specific TI and to zero for the other ones.

247   The probability map comes from a simple sketch (i.e. a pixelated image) given by the MPS

248   user. It is based on the geological concepts or interpretations that define the geometry

249   variability over the simulated area and that allow a partition of the outcrop. In each of the

250   zones defined in the area of interest, the simulated property will follow the intrinsic stationary

251   hypothesis (Gringarten and Deutsch, 2001; Journel and Zhang, 2006; Journel, 2005) but the

252   entire domain will be non-stationary.

253   While working on outcrops, the partition of the area of interest can be determined based on

254   observations. For instance, when the fracture network interpreted from outcrop images is

255   available, the geologist can visually define where the characteristics of the network are

256   changing (fracture orientation, intensity, length, topology) and draw limits around zones

257   where the network remains the same. However, in other cases outcrops or subsurface

258   observation could be discontinuous between observation sites. If the data are sparse and come

259   mainly from fieldwork ground observations or boreholes, the use of alternative statistical

260   approaches can help to provide a robust and accurate partition of the area of interest. The

261   work of Marrett et al., (2018) interprets the spatial organisation of fractures using advanced

262   statistical techniques such as normalized correlation count and weighted correlations count,

263   on scanlines collected in the Pennsylvanian Marble Falls Limestone. In their approach, the

264   periodicity of fracture spacing (clustering) calculated from the mentioned techniques is

265   evaluated using Monte Carlo to quantify how different the fracture networks are from a

266   random organisation. These approaches can be highly valuable during the process of building

267   a probability maps when less data are available. The probability maps provide a large-scale

268   framework that may be refined and modified with additional data such as measurement

269   stations or drone surveys coming from surface exploration or wells data containing fracture

270   network information.

271

272   **II.4 Testing the simulated network: from pixels to segments**

273   MPS realisations are produced as pixelated images. To evaluate the resulting fracture

274   network, pixels alignments corresponding to fractures are extracted as discrete straight-line

275   objects defined by a starting and an ending x, y coordinates. Fractures are separated from the

276   background and in different sets by automatic image classification methods. On grayscale

277   images, this is obtained by multilevel image thresholding through the Otsu's method (Otsu,

278 1979). On color images, fracture sets are classified based on their color components with the

279 k-means clustering algorithm built in MATLAB (Lloyd, 1982). Image classification gives in

280 output a series of binary images, one for each fracture set, where lineaments are represented

281 as foreground (Kovesi, 2000).

282

III] Results: test case on analogues of the Potiguar Basin, E Brazil

III.1 Geological setting

285 The Potiguar Basin is a rift basin located in the easternmost part of the Equatorial Atlantic

286 continental margin, NE Brazil (fig. 2). The basin is found both onshore and offshore (fig. 2).

287 The basin was generated after the initiation of the South American and African breakup

288 during the Jurassic - Early Cretaceous times. It was structured by a first NW-SE extension

289 stage latterly rotating to an E-W extensional direction (Costa de Melo et al., 2016). The rift

290 basin displays an architecture of horsts and grabens striking NE-SW and bounded towards the

291 east and south by major faults systems (de Brito Neves et al., 1984, fig. 2). The Potiguar

292 Basin displays three sedimentary sequences deposited since the early Cretaceous times (i.e.

293 syn- and post rift depositions). The last post-rift sequence was deposited from the Albian and

294 encompasses the Cenomanian-Turonian Jandaíra Formation. This formation consists of up to

295 700 m thick bioclastic calcarenites and calcilutites deposited in transgressive shallow marine

296 environment. The stress field affecting the Jandaíra Formation during the Campanian to the

297 Miocene compression was oriented N-S (Bertotti et al., 2017). From the Miocene to the

298 Quaternary the onshore part of the Potiguar basin was uplifted. Synchronously, a new stress

299 field was established trending to a NW-SE direction (Reis et al., 2013).

300

III.2 Outcrop data

302 The area of interest measures 2.1 × 1.3 km and is located about 25 km NE of the city of Apodi

in the Rio Grande Do Norte state (fig. 2). It contains two outcrops AP3 and AP4 (Bertotti et al., 2017; Bisdom, 2016, fig. 2) here defined respectively as 600×300 m and 400×500 m large pavements localized in the Jandaíra Formation. AP3 and AP4 crop out as pavements with no significant incision. The outcrops are sparsely covered by vegetation and consequently they present a clear fracture network highlighted by karstification. In 2013, images of AP3 and AP4 were acquired using a drone (Bisdom, 2016) and processed using the photogrammetry method. Two high-resolution ortho-rectified images of these pavements (centimetre-scale resolution) were used to complete fracture network interpretation and to extract fracture parameters. In AP3, 775 lineaments were traced (fig. 3) and in AP4, 2593 (fig. 4). These lineaments are grouped in this article over the general term "fractures". For each of these outcrops three fractures sets were identified: set1 striking N135-N165, set2 striking N000-N010/N170-N180 and set 3 striking N075-N105. Fractures falling outside of these ranges were not considered in the input data. Consequently, in AP3 we considered 562 only (out of 775 fractures traced in the pavement) and in AP4 we considered 1810 only out of 2594 fractures. In addition, ground-based fieldwork was conducted in AP3 and AP4 to understand the structural history of the area and to calibrate the interpretation conducted on the drone aerial photography (Van Eijk, 2014). General location and fracture data are presented in figure 3 and 4 and in table 1.

In AP3, sets 1 and 2 are evenly distributed over the pavement. However, they present intrinsic intensity variability in the area of interest. Set 3 is mainly expressed in distinct regions of the outcrop. Small-scale investigations (conducted on measurement stations in the outcrop) allowed associating set 3 with stylolite and sets 1 and 2 to veins. In addition, sets 1 and 2 present evidences of shear movements and are then considered as a conjugate system.

In AP4 small-scale investigations highlight the same characteristics as the ones observed in AP3. Although the conjugate system (set 1 and set 2) is less developed there than in AP3. It is

328 also notable that more crosscutting relationships were observed in AP4 compared to AP3.

329

III.3 Input data for MPS simulation

331 To evaluate the effect of conditioning data, results of two simulations were compared, with

332 and without conditioning data. The sensitivity of simulation parameters was investigated by

333 varying i) the number of neighbours defining patterns (data events d_n), ii) the acceptance

334 threshold (t) defining the tolerance the algorithm authorises to find a matching data event in

335 the simulation grid (Mariethoz et al., 2010) and iii) the fraction of the TI to be scanned during

336 the simulation process to search for data events. Results of this sensitivity analysis help to

337 propose the best possible simulation for AP3 and to optimise the choice of input parameters

338 for AP4 fracture simulation.

339 AP3 presents intrinsic fracture network geometry variability. This observation emphasizes

340 that averaging fracture parameters on the entire domain is not well suited to represent the

341 complexity of the network. We observed that the length of fracture per sets and the density of

342 fractures are parameters that vary the most here. The analysis of these variations allow to

343 partition AP3 and AP4 in elementary zones and to synthesize the fracture network

344 characteristics in each of these domains. The following section defines how the TI,

345 probability map and conditioning data were built.

346 ● **Partitioning, training images and probability map for AP3 and AP4**

347 We divided AP3 in 5 elementary zones (EZ) based on visual inspection of the pavement (fig.

348 5A-B). The number of fractures per EZ is synthesized in the figure 5. The proportion of

349 fracture per elementary zone is available in table 1. A limited part of the fractures belong to

350 two neighbours elementary zones. This issue is quantified in table 1.

351 A probability map with sharp boundaries (fig. 5B) was created for AP3. Sharp boundaries are

352 justified by the variability of the network geometry, which is known from the visual

inspection of the interpreted image. Smooth transitions could also be defined (see discussion). The input data to build the probability map is an image of the partition of the area of interest containing the different outcrops. In this image, the indexed zones (elementary zones EZ) are characterised by a distinctive colour.

At the scale of a reservoir where some outcrops analogues and fracture tracing may be available, the "interpreted reality" of the network can be directly used as a training image. We chose to ignore the tracing and to rely on parameters that are classically available without having access to drone images of an entire outcrop (i.e. orientation, spacing, abutment) and to compare the interpretation with the simulated network. In that respect fracture orientation were averaged to a single value. Hence, set 1 strikes N150, set 2 strikes N000 and set 3 strikes N090. According to the outcrop partitioning, five training images were created (fig. 5C). In each training image, three facies corresponding to the three fracture sets were created. Set1 (N090) is green, set 2 (N150) is red and set 3 (N000) is blue (fig. 5C). The topology is a crucial problem in fracture simulations because it influences the connectivity of the network. In the MPS simulations the abutments are particularly well reproduced as they represent singular pixels arrangements that are efficiently taken into account. However, crosscutting relationships imply the use of a different facies at the intersection locus. This method respects and reproduces intersections during the simulation process. In AP3, the analysis of the topology relationships showed three main crosscutting interactions:

-   Long N150 crosscut long N000 fractures (conjugated sets)

-   N000 crosscut N090

-   N150 crosscut N090

To take into account these topological parameters a different facies colour was attributed to the crosscutting locus (the crossing facies, fig. 6). When the MPS realization will be later discretized, the younger fractures will be truly represented as continuous segments. The older

378 fractures will be cut in pieces but their alignment will be, in most of the case, maintained

379 during the simulation process.

380 • **Dimensions of the simulation grids and of the training images**

381 The dimensions of the simulation grid for AP3 and of each training image (in pixels) are

382 shown in fig.5. The number of pixels is automatically determined by the size of the original

383 drawing made by the geologist.

384 The size of the input training image does not generally influence the simulation. However, it

385 has to be chosen sufficiently large with respect to the complexity of the patterns in order to

386 get reliable spatial statistics. The DS method tends to identify patterns (i.e. d_n's see above) in

387 the TI and to paste the central node of them into the simulation grid. However, at a constant

388 resolution and specifically for fractures patterns, it is likely that a 50×50 m training image

389 will carry more complexity and variability than a 10×10 m one. This parameter should be

390 taken into consideration when starting digitizing training images, especially when spacing

391 between fractures is not consistent across the simulation grid.

392 • **Long fractures conditioning**

393 Because the MPS method has the tendency to cut long individual segments into smaller

394 pieces, the fractures longer than 40 meters – the ones visible from satellite/drone imagery in

395 AP3 – where isolated and considered as hard conditioning data (fig. 5D). This threshold was

396 arbitrarily determined from the dataset we have. In AP3, less than 8% of the fractures are

397 longer than 40 m.

398 In AP3, long fractures belong only to the sets oriented/striking N000 or N150 (fig. 5D). 18

399 N000 fractures (3% of the whole) and 30 N150 fractures (5% of the whole) were digitized and

400 integrated as conditioning data in the simulation.

401

402 **III.4 Outcrop scale simulations**

III.4.1 Impact of conditioning data on AP3 simulations

In AP3, the 48 long fractures were manually digitized and imported into the simulation grid as categorical properties to be considered as hard conditioning data during the MPS simulation process. The MPS simulation is consequently in charge of stochastically populating the smaller factures within the grid.

Results of the influence of these data are presented in figure 7. The principal simulation parameters in the considered scenarios (with and without conditioning data) were set up identical (constant acceptance threshold (5%), constant percentage of scanned TI (25%) and constant number of neighbours (50)).

Results showed that the realisation without conditioning data creates 20% less fracture than the original outcrop reference. The simulation with conditioning data creates 9% less fractures than AP3, which makes the simulation satisfactory. It is also remarkable that the non-constrained simulation represents only 23 fractures above 40 meters (compared to the 48 long fractures interpreted on the AP3 outcrop). In this simulation the long fractures are essentially located in the zone 3 of the outcrop. Because the simulation is a stochastic process, the location of the long fractures is randomly determined in the absence of hard conditioning data. Considering hard-conditioning data also gives a more realistic representation of the fracture network.

III.4.2 Sensitivity analysis on the AP3 simulation parameters

- **Simulation parameter set-ups, duration and analyses conducted on the results**

Simulation parameters were varied for each simulation in order to emphasize their effect on each realisation. One realisation per test was performed during this analysis. The goal of this analysis is to show how the different parameters influence the reproduction of fracture

427 segments and not to evaluate how good is the matching between the simulation and the

428 reference.

429 The MPS realisations are pixelated images. The sensitivity analysis is based on the discrete

430 segments extracted from these pixelated images (see II.4). All of the simulations present a

431 variable percentage of segment lengths that are below the minimal fracture length interpreted

432 in the AP3 outcrop (i.e. simulation noise). Consequently all segments smaller than 2.2m

433 where removed from the simulation results. A length frequency distribution was compiled for

434 each of the generated simulations.

435 The influence of the number of neighbours was evaluated trough 7 simulations (SIM1 to

436 SIM7). The acceptance threshold and the number of neighbours was investigated by

437 comparing 8 simulations (SIM8 to SIM15) where the scanned fraction of the TI was fixed at

438 25%. The percentage of the scanned fraction of the TI was combined with the 2 other

439 simulation parameters. This combination was tested over 12 simulations (SIM16 to SIM27).

440 The models set-ups and the duration of the simulations are presented in (table 2). Tt is notable

441 that SIM8 / SIM9, SIM10 / SIM11 and SIM13 / SIM14 produce exactly the same network

442 despite the modification of the simulation parameters. Also The MPS algorithm successfully

443 performed SIM16 but the segment extraction generated an error preventing the discretisation

444 of all of the objects.

445 The total amount of generated fractures was counted and compared with the total number of

446 fractures interpreted from the original outcrop. A deviation of 10% compared to the original

447 amount of interpreted fractures is considered as a satisfactory result as it is very close to the

448 reference amount of fractures. A deviation of 20% compared to the original amount of

449 interpreted fractures is considered as an acceptable result. This deviation is consequent but

450 can be adjusted by varying the simulation parameters. A deviation above 20% was rejected as

451 a complete reconsideration of the parameters is required. Results are synthesized in table 3.

452 The total amount of segments was initially counted in the entire simulation domain. The sum

453 of segments per part is constantly higher than the initial total amount of segments because

454 segments cutting a sharp boundary are divided in two - segments falling within two

455 elementary zones and are consequently counted twice. The number of generated fractures per

456 simulation zone was also computed and the same deviation thresholds were applied to

457 evaluate if the simulation is satisfactory, acceptable or rejected. Tables 4 to 6 synthesize the

458 sensitivity analysis conducted of 27 realisations of the AP3 outcrop.

459 The length of the segments have been computed for each realisation and are presented in

460 figure 8.

461 The influence of the hard conditioning data and of the drawing of the training image was also

462 quantitatively investigated and compared respectively with the length of the generated

463 segments and with the amount of segments generated per zone.

464 • **Summary of the results**

465 Increasing the number of neighbours rises the computation time (table 2, SIM 1 to 7). A small

466 amount of neighbours results in a noisy simulation (table 2, SIM1). The contrary leads to a

467 downsampling of the generated segments that become longer than the interpreted fractures in

468 AP3 (table 2, SIM7). Decreasing the acceptance threshold leads to an increase of the

469 simulation time (table 2 SIM8-15). Increasing the scanned fraction of the TI is the most time

470 consuming operation (table 2 SIM17-27).

471 Increasing the number of neighbours only is generally not sufficient to accurately generate a

472 satisfactory or acceptable total amount of fractures (table 3). Increasing the scanned fraction

473 of the TI produces in all cases the closest total number of fractures compared to the reference

474 outcrop (table 3).

475 The counting of fractures in simulation zones revealed that set 2 and set 3 in zone 1, set 3 in

476 zone 4 and set 1 in zone 5 are generally underestimated during the simulation process. In

19

477 contrast, fracture set 1 in zone 2 is generally overestimated. The consistency of the error over

478 almost the entire set of simulations indicates an issue on the training image representation

479 (table 4-6). Increasing the scanned fraction of the TI generally allows to better represent a low

480 proportion of fracture facies within a TI (Zone TI5, set 2, table 6).

481 An acceptance threshold below 5% leads to an overestimation of the number of small

482 fractures (between 0-10 m), fig 8. In this case, amount of segments between 0-20 m is

483 generally close to the reality. Increasing the scanned fraction of the TI produces the highest

484 quantity of fractures ranging from 0-10 m (fig. 8). Increasing the number of neighbours and

485 the percentage of the scanned TI will result in an increase of the length of the fractures used

486 as hard conditioning data. However, the fracture elongation does not affect all of the hard

487 conditioned fractures and represents a very small percentage of the whole modelled fracture

488 network.

489

490   **III.4.3 Attempt at an optimisation: OPT1**

491 OPT1 was parameterised in regard of the previous observations in order to generate a

492 simulation that is the closest-to-reality possible. For this purpose, the amount of fractures

493 from set 2 and set 3 drawn in TI1 and set 3 drawn in TI4 was increased. In contrast, the

494 amount of fractures from set 1 drawn in TI2 was decreased significantly (fig. 9). We choose

495 to setup the number of neighbours at 50 and the acceptance threshold at 2%. TI1 and TI4 will

496 be scanned at 75% and the rest of the TIs will be scanned at 50% (table 2).

497 The simulation time for the proposed simulation is 2 min 31s (table 2). The total amount of

498 generated fractures is satisfactory compared to the amount of fractures interpreted in the

499 original outcrop.

500 To evaluate the robustness of the optimised simulation, 6 realisations using the same

501 parametrisation were generated for OPT1. The total amount of fractures generated for these

502 simulations always fall below the 10% deviation compared to the reference outcrop.

503 The number of segments comprised between 0-20 m in OPT1 is slightly above the

504 satisfactory deviation limit. As per all the generated simulations, the number of fractures

505 between 2.21 m and 10 m is largely overestimated.

506 OPT1 contains a more satisfactory and acceptable fracture count than any other simulation

507 generated before (table 6). The amount of segments generated in zone 1 and 2 for set 1 is

508 slightly overestimated. In zone 3, OPT1 fails to represent the amount of fractures for set 1

509 (25% deviation) and for set 3. Fracture set 1 in zone 4 is largely overestimated.

510

511 **III.4.4 Evaluation of the AP3 and OPT1 simulations: P_{21} calculations**

512 Uncertainty analysis is required when performing simulations of geological parameters,

513 especially far from data. The sensitivity analysis presented in this paper is a way to compare

514 the MPS simulations with the reference outcrop.

515 To reinforce the evaluation of the proposed method, we quantified the values of fracture

516 intensity in the reference outcrop, in three selected AP3 MPS simulations and in the optimised

517 simulation (OPT1) (fig. 10). The fracture intensity was classified by Dershowitz and Herda,

518 (1992) in regard of i) the size and dimension (1D, 2D, 3D) of a selected zone of interest and

519 ii) the number, length, area or volume of fractures within this selected zone. In this paper, we

520 chose to calculate the P_{21} fracture intensity, which corresponds to the sum of all fracture

521 lengths within a regularly discretized spaced, with constant area boxes (10×10 m) covering

522 the entire AP3 area of interest.

523 Visually, the results show an apparent higher P_{21} intensity in the reference outcrop than in the

524 simulations. However, zones of high intensity in the reference outcrop are generally well

525 represented in SIM26 and in OPT1. This is in agreement with the results of the sensitivity

526 analysis showing that SIM26 and OPT1 best represent the number of fractures present in the

527 reference outcrop.

528 The average fracture intensity in each simulation has also been computed and confirms the

529 observations conducted during the sensitivity analysis. SIM1 and SIM7 present the lowest

530 average fracture intensity (0.095 m^{-1} and 0.079 m^{-1} respectively) and SIM26 and OPT1

531 present the highest fracture intensity (0.11 m^{-1} and 0.099 m^{-1} respectively). The average

532 fracture intensity in the reference outcrop is higher than in any other simulations (0.126 m^{-1}).

533 However, this value remains close to the ones obtained in SIM26 and OPT1.

534 The fact that the fractures have been simplified as straight lines in the simulations combined

535 to a relatively small area of calculation (10×10 m) could be one element of explanation of

536 the observed fracture intensity variation between the reference outcrop and SIM26 and OPT1.

537 This analysis strengthens the results obtained during the sensitivity analysis and demonstrates

538 the capacity of the MPS method to represent with a high fidelity the geometry of a fracture

539 network.

540

541 **III.4.5 Using the sensitivity analysis results to model AP4**

542 As per AP3, AP4 present an intrinsic variability of the fracture network geometry. This

543 outcrop was divided in 3 elementary zones (fig. 11A-B). According to AP4 partitioning, a

544 probability map with sharp boundaries (fig. 11B) was created. For AP4, the configuration of

545 the outcrop led to mask the area where no interpretation data were performed. In these

546 particular zones a "no data value" was attributed and these masked areas were excluded

547 during the modelling process. In AP4 three training images were created (fig. 11C). As per

548 AP3, the size of the AP4 simulation grid was doubled compared to its original dimension

549 (available in fig.11). In AP4, fractures longer than 40 meters were also considered as hard

550 conditioning data. Here, less than 1.5% of the fractures are longer than 40m (fig. 11D). In

551 AP4, long fractures were found in the 3 sets and mainly in the south-eastern part of the

552 outcrop (fig. 11D, elementary zone 6). 11 N000 fractures (0.5% of the whole), 13 N150

553 fractures (0.6% of the whole) and 9 N090 fractures (0.4% of the whole) were digitized and

554 integrated as conditioning data into the simulation.

555 Based on the results of the sensitivity analysis of AP3 we generated one simulation for the

556 AP4 outcrop (fig. 12). The modelling parameters for SIM AP4-1 were selected as following:

557 the number of neighbours was set up at 50 and the acceptance threshold at 2%. The 3 training

558 images used in the simulation are presented in figure 12 and are considered as representative

559 of the fracture arrangement in each region of the simulation. The scanning percentage of TI6

560 and TI7 was set up at 50%. The scanning percentage of TI8 was set up at 100%. With this

561 configuration, the simulation lasts slightly more than 5 minutes. The fact of intensely

562 scanning TI8 is probably responsible of this duration. The analysis was conducted on the total

563 amount of segments generated and of segments per set of fractures. In AP4 the total number

564 of segments is 1810. The simulation realises 1682 segments in total, which constitutes a

565 satisfactory result. The original AP4 presents 252 segments striking N150 (set 1), 856

566 segments striking N000 (set 2) and 702 segments striking N090 (set 3). The results of

567 simulation AP4-1 are always satisfactory or acceptable with 206 segments striking N150 (set

568 1), 834 segments striking N000 (set 2) and 642 segments striking N090 (set 3). A detailed

569 analysis was not conducted here because AP4 contains a lot of small fracture intersections

570 (especially in the TI8 zone) and this makes the segment extraction a complex process.

571 However, these results are promising for the future.

572

573 **IV] Smooth transitions between elementary zones: towards reservoir scale**

574 **models to manage uncertainties**

575   The strength of the method proposed here relies on the use of a probability maps and on the

576   opportunity to consider multiple training images in a single realisation to generate non-

577   stationary models of fracture network geometries. In the case of AP3 and AP4, the probability

578   maps are essentially constrained by the variation of geometry of the fracture networks

579   observed on the geological interpretation made on the drone imagery. Consequently, the

580   defined areas are pragmatically bounded and the nature of the limit between one zone and

581   another is a sharp boundary.

582   AP3 and AP4 outcrops are separated by about 2.5 km and very little is known about the

583   fracture network geometry between these two locations. Assuming that there is no major

584   structural deformation (fold or faults) that may cause a change in fracture geometry at the

585   close vicinity of the outcrop "reality", the zones initially defined on the AP3 and AP4 outcrop

586   can be extended to the limits of the reservoir-scale model boundaries (fig. 13). In this

587   particular case, filling the gap between the two outcrops appears to define how the transition

588   between one side of the simulation grid and the other should be determined.

589   Fractures are localised objects that do not need to be necessarily continuous from one

590   simulation zone to another. The constant higher proportion of the non-fractured matrix facies

591   versus localised and thin fracture elements ensures the coherency and relative compatibility

592   from one simulation region to another. The idea of the simulation grid region partitioning was

593   re-evaluated and an alternative method, was proposed here. Contrarily to the definition of

594   sharp boundaries in the probability maps used for AP3 and AP4, a probability map with

595   smooth transitions is defined as follows. An ensemble of elementary zones covering a part of

596   the simulation grid is defined. Each TI corresponds to one elementary zone, which is

597   simulated using exclusively that TI. The probabilities in these zones are then set to one for a

598   specific TI and to zero for the other TIs. The remaining part of the simulation grid is divided

599   in transition zones, for which one has to define which TIs may be involved. In a transition

600 zone, the probabilities of the involved TIs are set proportional to the inverse distance to the

601 corresponding elementary zones. This process creates smooth transitions in low constrained

602 area decreasing the influence of one TI towards another (from one elementary zone to

603 another).

604 No faults or folds can be initially identified between AP3 and AP4 to condition the drawing of

605 the probability map. In this case, a rectangular compartment representing a gradual

606 probability transition to use the training image associated to one outcrop or to the other filled

607 the blank space between the two outcrops. For instance, fig 13E shows in the

608 Transition_Zone_1 a decreasing probability to use TI1 from left to right (i.e. zone 1 to zone 6)

609 and conversely to use TI6 from right to left.

610 Recently, investigations conducted on the Rio Grande do Norte geological map (Angelim et

611 al., 2006), demonstrated the presence of a fault crossing the simulation grid near the AP3

612 zone. This structure may explain the variability of fracture geometry from AP3 (EW stylolites

613 and strong presence of conjugated NS/NW-SE system) to AP4 (EW stylolites associated to

614 NS fracture system, the NW-SE conjugated system is here subordinate). Further geological

615 investigations need to be conducted in this particular place to proof the influence of this fault

616 on the network geometry. However, fig 13F shows an alternative probability map taking into

617 account this interpretation and present how flexible the probability map can be. The proposed

618 method demonstrates its adaptability in various geological contexts.

619

620 **V] A method to create a 3D DFN out of 2D MPS realisations**

621 The MPS simulations presented in this paper are on the form of 2D pixelated maps.

622 MATLAB codes were developed to extract starting and end point coordinates (georeferenced)

623 of a series of aligned colorized pixels that represent a fracture trace from these images.

624 Transforming this output in geologically realistic 3D surfaces is not easy. Karimpouli et al.,

(2017) studied samples coming from coalbed methane reservoirs in the fractured Late Permian Bowen Basin in Australia. They realised multiple 2D and pseudo 3D images (i.e. orthogonal 2D images) and used the cross-correlation based simulation (CCSIM) to represent the internal organisation of coal cleats and the heterogeneity of the coal matrix in 3D. Their approach greatly improved the understanding of the internal complexity of coal samples and gives better results than classical DFN's based on averaged distributions. However, their method requires an important initial amount of information (i.e. CT scans slices used as training images) that is generally not available at a larger scale. The use of MPS in 3D seems particularly not suited for fracture network representation because: i) they require to associate fractures from 2D map view and from 2D section view (3D or pseudo-3D), ii) it appears difficult to consider isolated fractures in this type of approach and iii) in the subsurface fracture height and/or fracture length are generally unknown.

To Tackle these problems we choose to use multiple 2D MPS-generated fracture networks. In the presented approach, the 3D is obtained by extruding 3D fracture planes in fracture units (fig. 14). In this approach we consider that fractures are entirely bound to the units, which can appear as a limitation if isolated fractures occurs inside a layer. However, we can consider variable levels of fracture units. Figure 14 presents an hypothetic scenario where red fractures are confined to a large fracture unit (FU1) crosscutting smaller ones (FU4 containing also smaller red fractures). In such a representation, one 2D planar simulation is required at each top mechanical unit to generate a new set of fractures.

In real-world subsurface configurations, mechanical units can be extracted from well logs (resistivity, density, lithology; Laubach et al., 2009). The fracture height distribution, referred as fracture stratigraphy (Hooker et al., 2013) requires here a particular attention and is difficult to extract from borehole data. In outcrops, the use of vertical cliffs adjacent to 2D horizontal pavement should be a way to evaluate these heights and to constrain the 3D model.

650   In outcrops, the resort to vertical cliffs adjacent to 2D horizontal pavements is required to

651   define fracture height. This method is already implemented in gOcad-SKUA software as a

652   macro that extrudes planes of a single fracture family (i.e. all the red fractures in AP3)

653   vertically into a bounded volume (fig. 14). More developments are in process to generate

654   oblique planes and to be able to extrude planes in portions of the fracture sets.

655

V] Conclusions

657   In this paper a new method to predict the geometry of a natural fracture network using the

658   multiple-point statistic algorithm is presented. The method provides stochastic realisation

659   depicting a realistic non-stationary fracture network arrangement in 2D based on the use of

660   multiple, simplified, small training images capturing the natural fracture attributes in specific

661   zones defined by a probability map. Probability maps are adaptable and follow geological

662   rules of fracture type and arrangement distribution specific to various tectonic contexts (i.e.

663   faulting, folding and poor deformation context/no fault, no folds). We developed methods to

664   be able to consider transition zones into the probability maps (e.g. zones far from hard data)

665   that allow simulating fracture network geometry at a larger scale (i.e. reservoir scale).

666   The realisations obtained from 2D MPS constitute a statistical laboratory close enough to the

667   reality to be tested in terms of fracture mechanical parameters and response to flow.

668   Comparison between mechanical aperture calculation, fluid flow simulations conducted on

669   both "reality" fracture network interpretations performed on drone imagery and series of MPS

670   realisations gives similar results.

671   The method proposed here is applicable to all rock types and to a wide range of tectonic

672   contexts. Initially calibrated using outcrop data, the method is fully adaptable to the

673   subsurface in order to better characterise fractures in water, heat or hydrocarbon reservoirs.

674   The challenge there, remains on the definition of the different training images on which the

simulation is based. Very few data is generally available in the subsurface and geological rules need to be found to define the geological characteristics of the fracture network (orthogonal or conjugate network) and the associated fracture attributes (length, height, spacing, density, topology).

Acknowledgments

Appendix A

The DeeSse algorithm (Straubhaar et al., 2011) was used in this paper to reproduce existing fracture network interpreted from outcrop pavements. The following pseudocode developed by Oriani et al., (2017) have been modified to explain how the algorithm is processing the simulation of fracture. Specific terms can be found in section II.1 of the present paper. In our study the simulation follows a random path into the simulation grid. This grid is step by step

700   populated by values (fracture facies in our case) sampled in the training image. The algorithm

701   proceeds according to the following sequence :

702   1. Selection of a random location x in the simulation grid that has not yet been simulated

703   (and not corresponding to conditioning data points, already inserted in the grid).

704   2. To simulate $V(x)$ → the fracture facies into the simulation grid: The pattern $d_n(x) =$

705    $(x_1, V(x_1)), ..., (x_n, V(x_n))$ formed by at most n informed nodes the closest to x is retrieved.

706   If no neighbours is assigned (at the beginning of the simulation), $d_n(x)$ will then be empty:

707   in this case, assign the value $V(y)$ of a random location y in the TI to $V(x)$, and repeat the

708   procedure from the beginning.

709   3. Visit a random location y in the TI and retrieve the corresponding data event $d_n(y)$.

710   4. Compare $dn(x)$ to $dn(y)$ using a distance $D(dn(x), dn(y))$ corresponding to a measure of

711   dissimilarity between the two data events.

712   5. If $D(dn(x), dn(y))$ is smaller than a user-defined acceptance threshold T, the value of

713    $V(y)$ is assigned to $V(x)$. Otherwise step 3 to step 5 are repeated until the value is assigned

714   or an given fraction F of the TI, is scanned.

715   6. if F is scanned, $V(x)$ is defined as $V(y)$, with y the scanned location minimising the

716   distance $D(dn(x), dn(y))$.

717   7. Repeat the whole procedure until all the simulation grid is informed.

718
719

720   **Figure captions**

721   **Figure 1:** Direct Sampling method workflow applied to fracture network modelling (modified
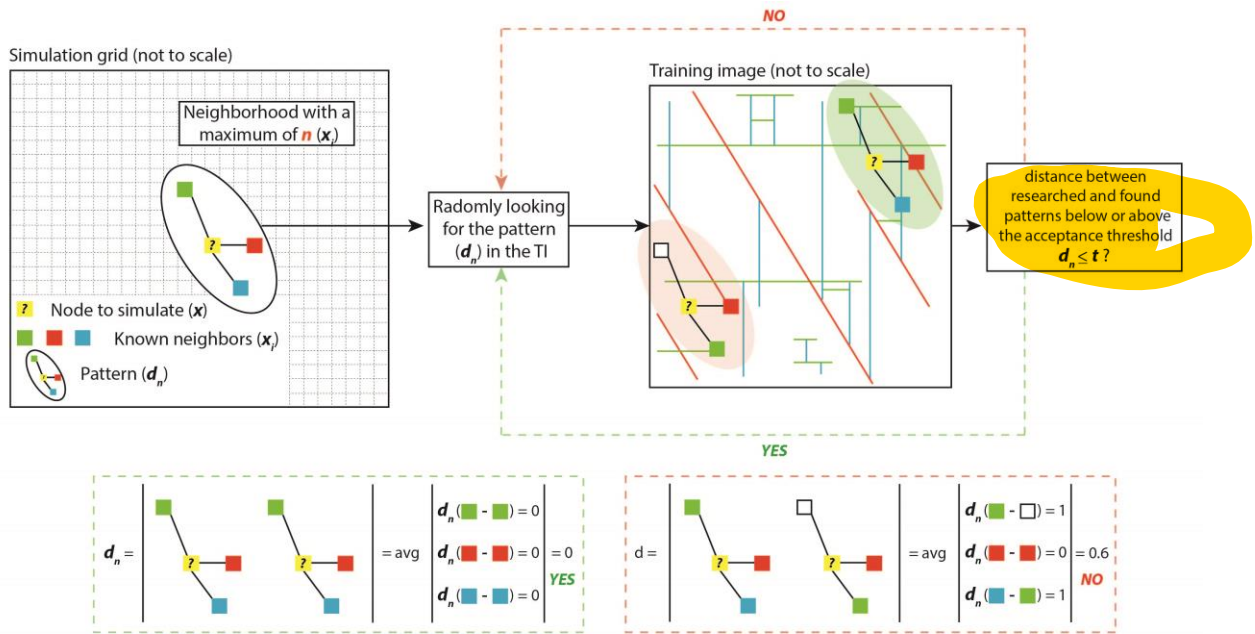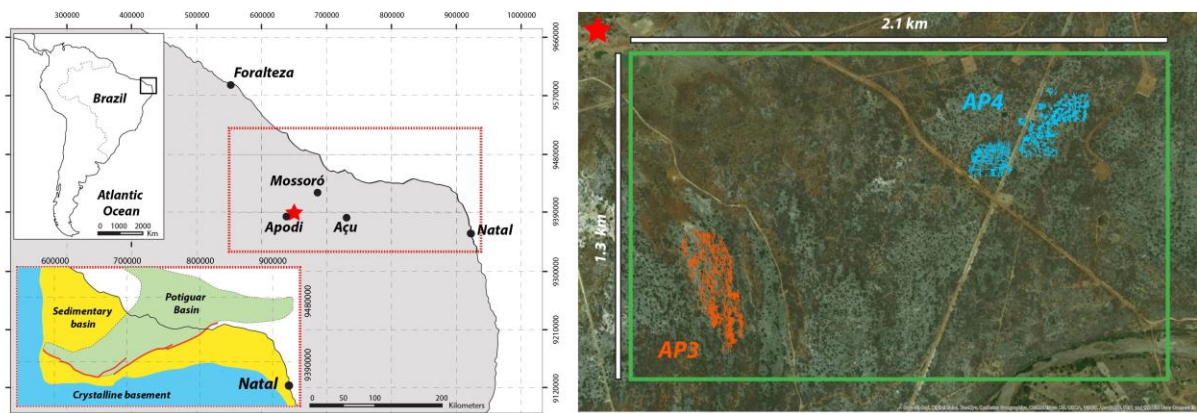
722   from Meerschman et al., 2013).

723

724

Figure 2: Location of the area of interest and of the studied pavements near Apodi area (red star).

727

728

729

730

731

Table 1: Outcrop characteristics and fracture parameters collected in AP3 and AP4

AP3 outcrop

Localisation (WGS84 UTM Z24S)		Orientation	Dimension		Fractures proportion (of the whole fracture population)			Fracture length	
X	Y		NS (m)	EW (m)	Set 1 (N135-N165)	Set 2 (N000-N010/N170-180)	Set3 (N075-N105)	Min (m)	Max (m)
650601	9387908	NNW-SSE	600	300	30%	52%	18%	2,21	123

					Elementary zone 1	Elementary zone 2	Elementary zone 3	Elementary zone 4	Elementary zone 5	Elementary zone 1	Elementary zone 2	Elementary zone 3	Elementary zone 4	Elementary zone 5	Elementary zone 1	Elementary zone 2	Elementary zone 3	Elementary zone 4	Elementary zone 5
					60%	26%	18%	70%	87%	37%	14%	80%	23%	13%	3%	60%	2%	7%	0%

AP4 outcrop

Localisation (WGS84 UTM Z24S)		Orientation	Dimension		Fractures proportion (of the whole fracture population)			Fracture length	
X	Y		NS (m)	EW (m)	Set 1 (N135-N165)	Set 2 (N000-N010/N170-180)	Set3 (N075-N105)	Min (m)	Max (m)
652032	9388508	NE-Sw	400	500	20%	40%	40%	1	186

|					Elementary zone 6	Elementary zone 7	Elementary zone 8	Elementary zone 6	Elementary zone 7	Elementary zone 8	Elementary zone 6	Elementary zone 7	Elementary zone 8
					8%	20%	10%	43%	45%	53%	49%	35%	37%

745 **Figure 3:** Data acquired in the area of interest in pavements AP3. A) ortho-rectified high-resolution pavement aerial images acquired with a

746 drone, B) fracture interpretation on ortho-rectified images, C) fracture orientation calculated from the north in GIS-based environment.

747 Corresponding rose diagram for both outcrops, D) length of each fracture trace and E) fracture topology relationship for each pavement observed

748 on fracture network interpretation.

749

750

751

752
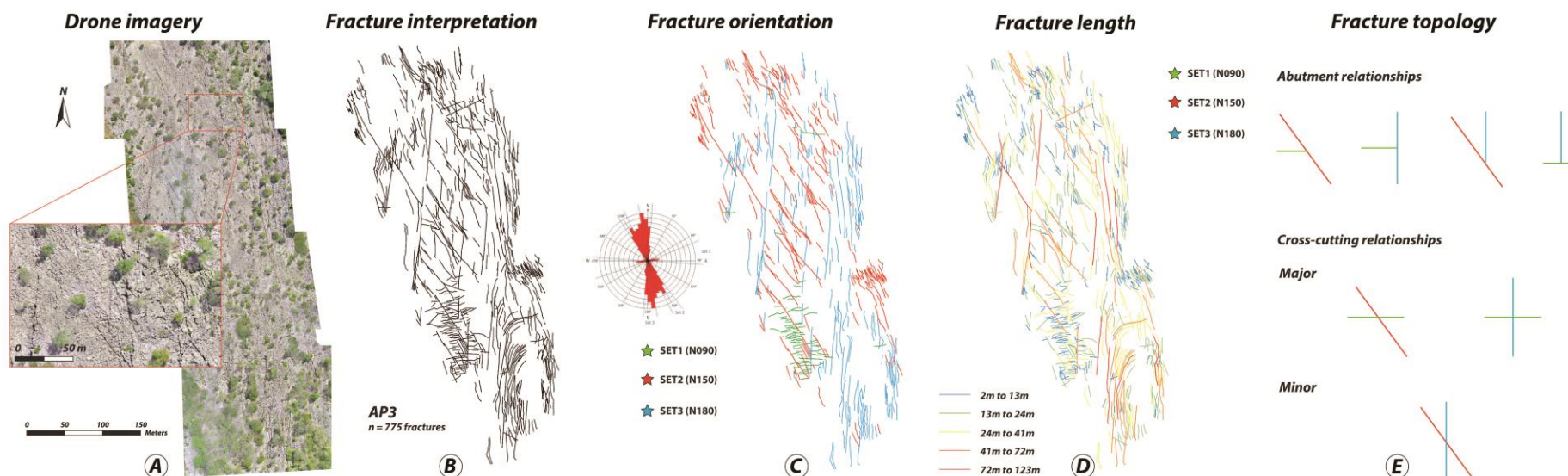
753 **Figure 4:** Data acquired in the area of interest in pavements AP4. F) ortho-rectified high-resolution pavement aerial images acquired with a

754 drone, G) fracture interpretation on ortho-rectified images, H) fracture orientation calculated from the north in GIS-based environment.

755 Corresponding rose diagram for both outcrops, I) length of each fracture trace and J) fracture topology relationship for each pavement observed

756 on fracture network interpretation
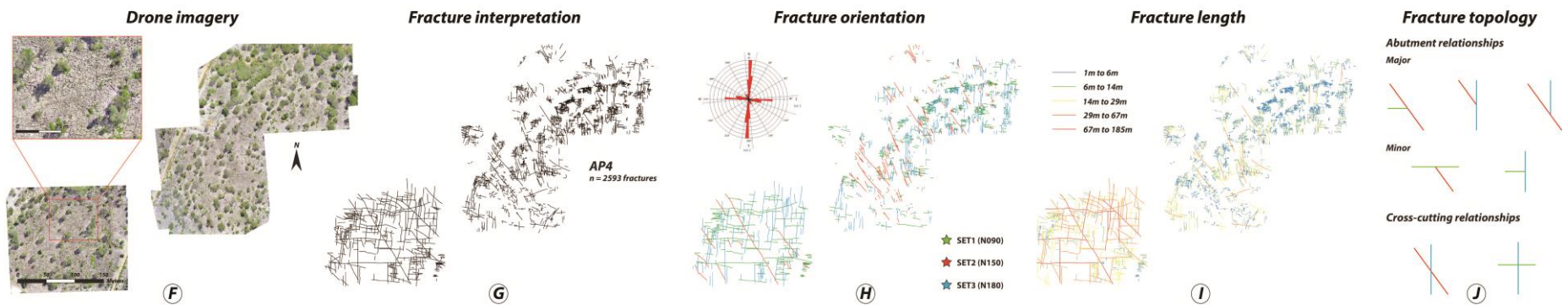
757

758

759

760

761

762

Figure 5: A) Partitioning of AP3 in 5 elementary zones (EZ). This partition is defined (with respect to fracture orientation (fracture facies), fracture density and geometry variability over the entire simulation domain. B) probability map and associated statistics for each EZ. C) training images associated with the partition of AP3. In each EZ, the corresponding training image has a probability (pTI) of 1 to be used. In this zone the other training images are not used (pTI = 0). D) hard conditioning data for AP3. All the fractures longer than 40 m are considered deterministically in the simulation process
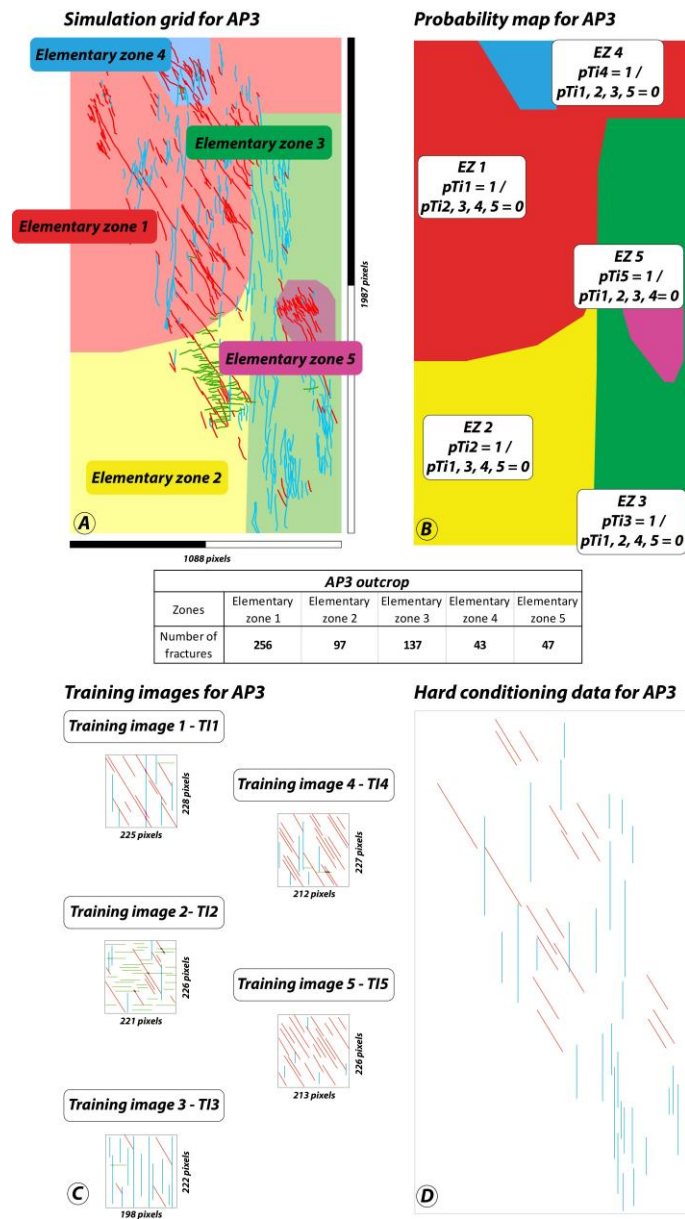
771   **Figure 6:** Comparison between results obtained without constraining the topology and with

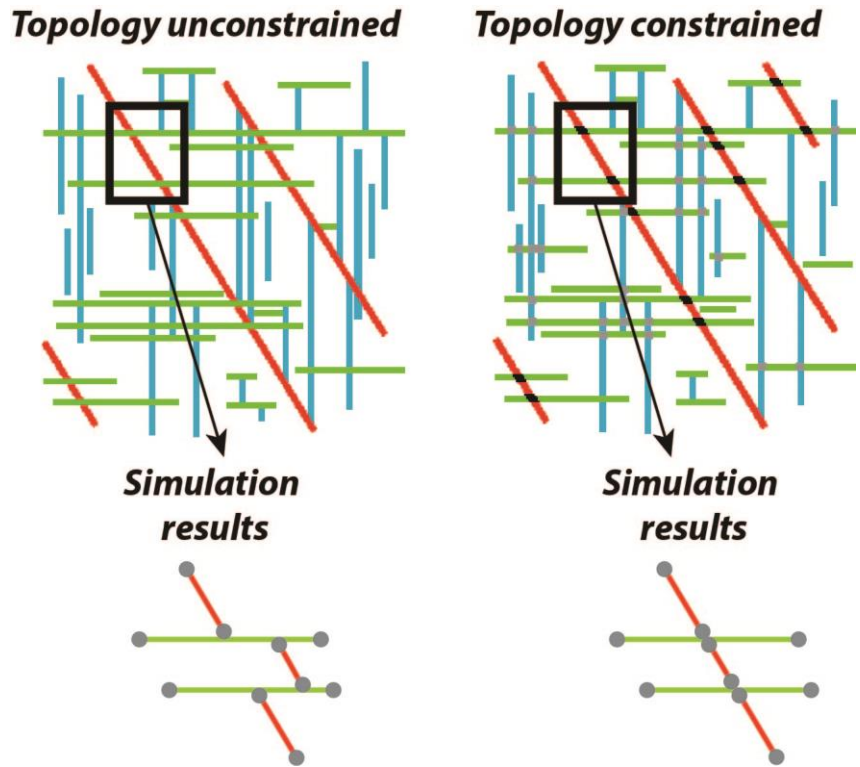772   topological facies constraints.

773

774

775   **Figure 7:** Visual comparison between: A) the reference fracture network interpretation (AP3),

776   B) the extraction of the longer segments (50 fracture longer than 40m), C) a simulation

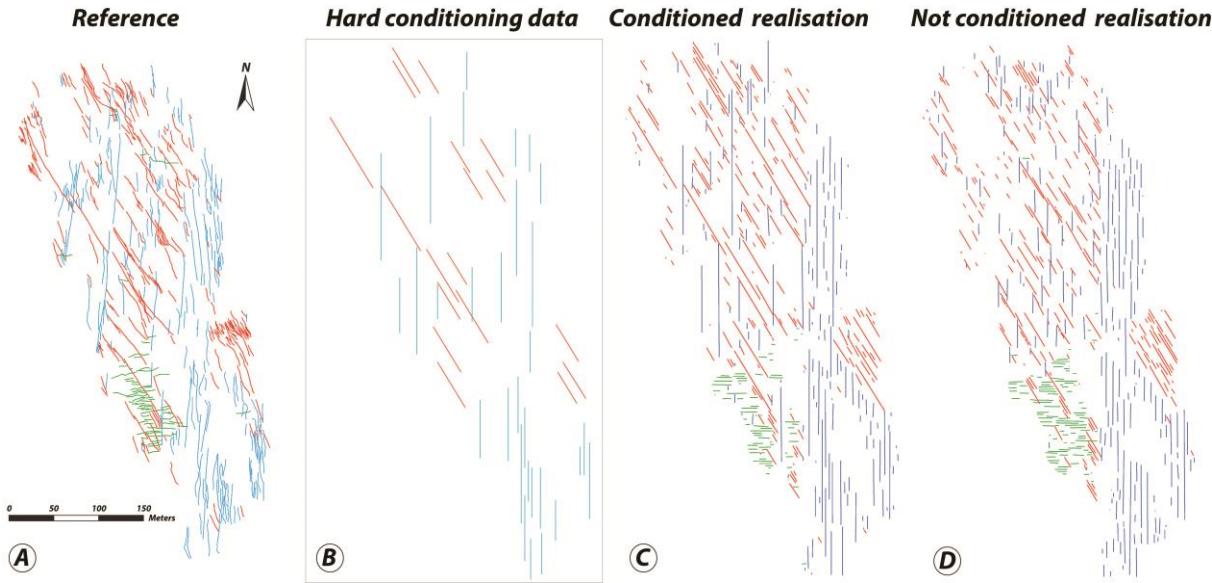777   conditioned by the long segments, D) a simulation not conditioned by the long segments

778

Table 2: Simulation parametrisation, models set-ups and duration of each run.

Tested parametrisation	Number of neighbours influence							Number of neighbours + Acceptance threshold							
Realisation name	SIM1	SIM2	SIM3	SIM4	SIM5	SIM6	SIM7	SIM8	SIM9	SIM10	SIM11	SIM12	SIM13	SIM14	SIM15
Simulation parameters	A. th. = 5% N. = 10 Scan= 25%	A. th. = 5% N. = 20 Scan= 25%	A. th. = 5% N. = 30 Scan= 25%	A. th. = 5% N. = 40 Scan= 25%	A. th. = 5% N. = 50 Scan= 25%	A. th. = 5% N. = 75 Scan= 25%	A. th. = 5% N. = 100 Scan= 25%	A. th. = 4% N. = 40 Scan= 25%	A. th. = 3% N. = 40 Scan= 25%	A. th. = 2% N. = 40 Scan= 25%	A. th. = 1% N. = 40 Scan= 25%	A. th. = 4% N. = 50 Scan= 25%	A. th. = 3% N. = 50 Scan= 25%	A. th. = 2% N. = 50 Scan= 25%	A. th. = 1% N. = 50 Scan= 25%
Simulation duration	22"	19"	33"	36"	55"	101"	136"	52"	52"	90"	95"	56"	76"	76"	121"

Tested parametrisation	Number of neighbours + Acceptance threshold + % TI scan												Optimisation
Group	Group 1				Group 2				Group3				
Realisation name	SIM16	SIM17	SIM18	SIM19	SIM20	SIM21	SIM22	SIM23	SIM24	SIM25	SIM26	SIM27	OPT1
Simulation parameters	A. th. = 3% N. = 40 Scan= 50%	A. th. = 2% N. = 40 Scan= 50%	A. th. = 3% N. = 50 Scan= 50%	A. th. = 2% N. = 50 Scan= 50%	A. th. = 3% N. = 40 Scan= 75%	A. th. = 2% N. = 40 Scan= 75%	A. th. = 3% N. = 50 Scan= 75%	A. th. = 2% N. = 50 Scan= 75%	A. th. = 3% N. = 40 Scan= 100%	A. th. = 2% N. = 40 Scan= 100%	A. th. = 3% N. = 50 Scan= 100%	A. th. = 2% N. = 50 Scan= 100%	Custom
Simulation duration	80"	148"	123"	124"	105"	196"	152"	154"	104"	203"	150"	149"	151"

Table 3: Comparison between the total amount of segments interpreted in the reference outcrop and in the different sets of simulations (tested parametrisation). Evaluation of the results in terms of satisfactory (green symbol), acceptable (orange symbol) or non-satisfactory (red symbol)

	Reference outcrop	Tested Parametrisation	Number of tested configurations	Results evaluation		
				✔	≈	✘
Total segments	562	Influence of the number of neighbours	n=7	1	1	5
		Number of neighbours + Acceptance threshold	n=8	3	2	3
		Number of neighbours + Acceptance threshold + % TI scan	n=12	5	6	1

Table 4: Results of the sensitivity analysis on the influence of the number of neighbours. The table presents the number of segments per simulation zone for AP3 (used as reference). Red symbols show a total amount of segments of the considered set in the considered zone deviating to more than 20% from the reference case. Yellow symbols show a deviation of more than 10% from the reference case. Green symbols do not deviate significantly from the reference outcrop interpretation.

		Reference	Number of neighbours						
			SIM1	SIM2	SIM3	SIM4	SIM5	SIM6	SIM7
		Segments per parts							
Zone TI1	Set1	156	✗	≈	≈	✗	✗	✗	✗
	Set2	95	✗	✗	≈	✗	✗	✗	✗
	Set3	6	✗	✗	✗	✗	✗	✗	✗
Zone TI2	Set1	22	✗	✗	✗	✗	✗	✗	≈
	Set2	12	✗	✗	✔	✗	✗	✗	✗
	Set3	57	✗	≈	✔	✔	✔	≈	✔
Zone TI3	Set1	20	✗	✔	✗	✗	✗	✗	✗
	Set2	113	✗	≈	✔	≈	≈	✗	✗
	Set3	2	✗	✗	✗	≈	≈	✗	✗
Zone TI4	Set1	25	✗	✗	✗	✔	✔	≈	✗
	Set2	10	✔	✔	✔	✔	≈	≈	≈
	Set3	3	✗	✗	✗	✗	✗	✗	≈
Zone TI5	Set1	39	✔	≈	✗	✗	✗	✗	✗
	Set2	2	✗	✗	✗	✗	✔	✔	≈
	Set3	0	✔	✔	✔	✔	✔	✔	✔
		Satisfactory total	No	Yes	Yes	No	No	No	No
		# satisfactory	3	3	5	4	4	2	4
		# acceptable	0	4	2	2	3	3	2
		# not acceptable	12	8	8	9	8	10	9

Table 5: Results of the sensitivity analysis on the influence of the number of neighbours and of the variation of the acceptance threshold. The colour code is the same as the one used in table 4.

		Reference	SIM8	SIM9	SIM10	SIM11	SIM12	SIM13	SIM14	SIM15
			Number of neighbours + Acceptance threshold							
			Segments per parts							
Zone TI1	Set1	156	✔	✔	≈	≈	✘	✔	✔	✔
	Set2	95	✘	✘	✘	✘	✘	✘	✘	✘
	Set3	6	✘	✘	✘	✘	✘	✘	✘	✘
Zone TI2	Set1	22	✘	✘	✘	✘	✘	✘	✘	✘
	Set2	12	≈	≈	✔	✔	✘	✘	✘	✘
	Set3	57	✔	✔	✘	✘	✔	✔	✔	≈
Zone TI3	Set1	20	✘	✘	✔	✔	✘	✘	✘	✘
	Set2	113	✔	✔	≈	≈	≈	✔	✔	≈
	Set3	2	≈	≈	✔	✔	≈	✘	✘	✔
Zone TI4	Set1	25	✔	✔	✘	✘	✔	✔	✔	✔
	Set2	10	✘	✘	≈	≈	≈	≈	≈	✔
	Set3	3	✘	✘	✘	✘	✘	✘	✘	✘
Zone TI5	Set1	39	✘	✘	✘	✘	✘	✘	✘	✘
	Set2	2	≈	≈	≈	≈	✔	≈	≈	≈
	Set3	0	✔	✔	✔	✔	✔	✔	✔	✔
		Satisfactory total	*Yes*	*Yes*	*Yes*	*Yes*	*No*	*No*	*No*	*Yes*
		# satisfactory	5	5	4	4	4	5	5	5
		# acceptable	3	3	4	4	6	2	2	3
		# not acceptable	7	7	7	7	9	8	8	7

Table 6: Results of the sensitivity analysis on the influence of the number of neighbours, of the variation of the acceptance threshold and of the variation of the percentage of the scanned fraction of the training image. The colour code is the same as the one used in table

		Reference	SIM16	SIM17	SIM18	SIM19	SIM20	SIM21	SIM22	SIM23	SIM24	SIM25	SIM26	SIM27	OPT1
				Number of neighbours + Acceptance threshold + % TI scan											Optimisation
				Group 1			Group 2				Group3				
				Segments per parts											OPT1
Zone TI1	Set1	156		✔	✔	✔	✔	✘	✔	✔	✔	✘	✔	✔	✘
	Set2	95		✘	✘	✘	✘	≈	✘	✘	✘	≈	✘	✘	✔
	Set3	6		✘	✘	✘	✘	✘	✘	✘	✘	✘	✘	✘	✔
Zone TI2	Set1	22		✘	✘	✘	✘	✘	✘	✘	✘	✘	✘	✘	✘
	Set2	12		✘	✘	✘	✘	✘	✘	✘	✔	✘	✔	✔	✔
	Set3	57		✔	✔	✔	✔	≈	✔	✔	✔	≈	✔	✔	≈
Zone TI3	Set1	20		✘	✘	✘	✔	✘	✘	✘	≈	✘	✔	✔	✘
	Set2	113		✔	✔	✔	≈	✔	✔	✔	✔	✔	≈	≈	✔
	Set3	2		≈	≈	≈	✘	✔	✔	✔	≈	≈	✘	✘	✘
Zone TI4	Set1	25		✘	✘	✘	≈	✘	✔	✔	✘	✘	≈	≈	✘
	Set2	10		✔	✔	✔	≈	✔	✔	✔	✘	≈	✔	✔	✔
	Set3	3		✘	✘	✘	✘	✘	✘	✘	≈	✘	✘	✘	✔
Zone TI5	Set1	39		≈	≈	≈	✘	✘	✘	✘	✔	≈	✘	✘	≈
	Set2	2		≈	≈	≈	✘	✘	✔	✔	✔	≈	✔	✔	✔
	Set3	0		✔	✔	✔	✔	✔	✔	✔	✔	✔	✔	✔	✔
		Satisfactory total		*Yes*	*Yes*	*Yes*	*No*	*No*	*Yes*	*Yes*	*Yes*	*Yes*	*Yes*	*Yes*	*Yes*
		# satisfactory		5	5	5	4	4	8	8	6	2	7	7	8
		# acceptable		3	3	3	3	2	0	0	3	7	2	2	2
		# not acceptable		7	7	7	8	9	7	7	6	6	6	6	5

819   **Figure 8:** Fracture length distributions tested during the sensitivity analysis. A) fracture

820   length distribution for SIM1 to SIM7, B) fracture length distribution for SIM10, SIM12,

821   SIM13, SIM15 and C) fracture length distribution for SIM16, SIM17, SIM20, SIM21, SIM22,
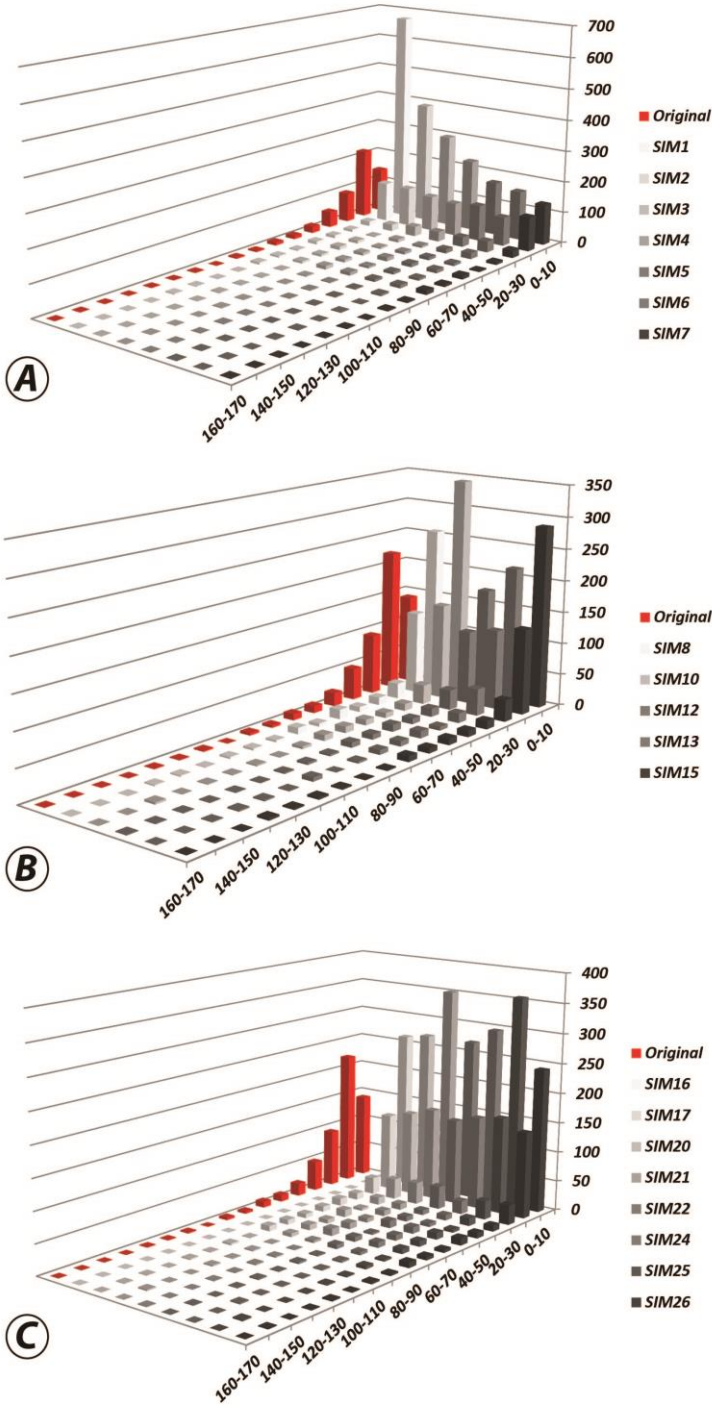
822   SIM24, SIM5, SIM26.

823

824　**Figure 9:** Comparison of the training images 1, 3 and 4 used during the sensitivity analysis
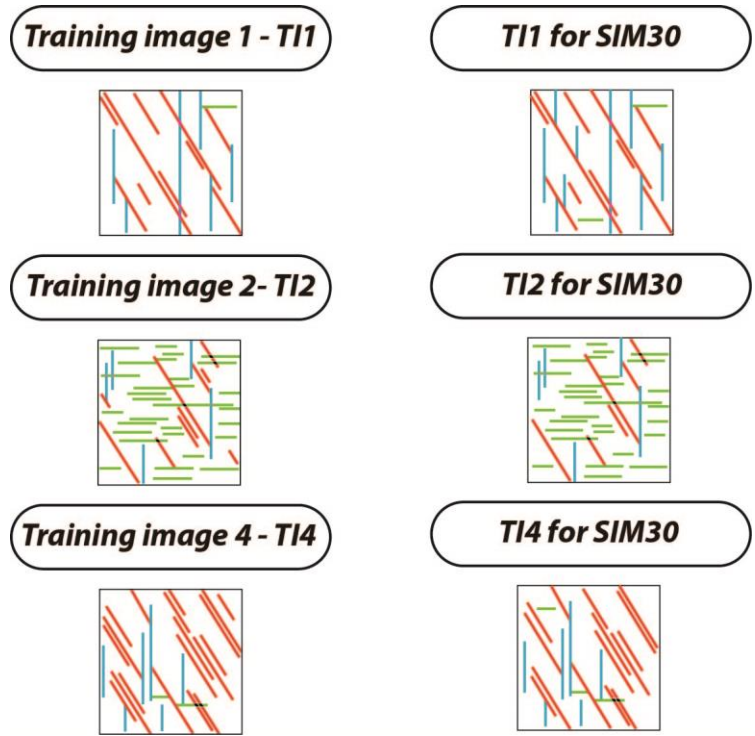
825　(27 simulations) and their modification for SIM 3

826

827

828

829

830

831

832

833

834

835

836

837

838

839

840   **Figure 10:** Comparison of the fracture intensity (P_{21}) calculated in the reference outcrop and

841   in four select MPS simulations

842

843

844

845

846

847

848

849

850

851

852

853

854

855

856

857
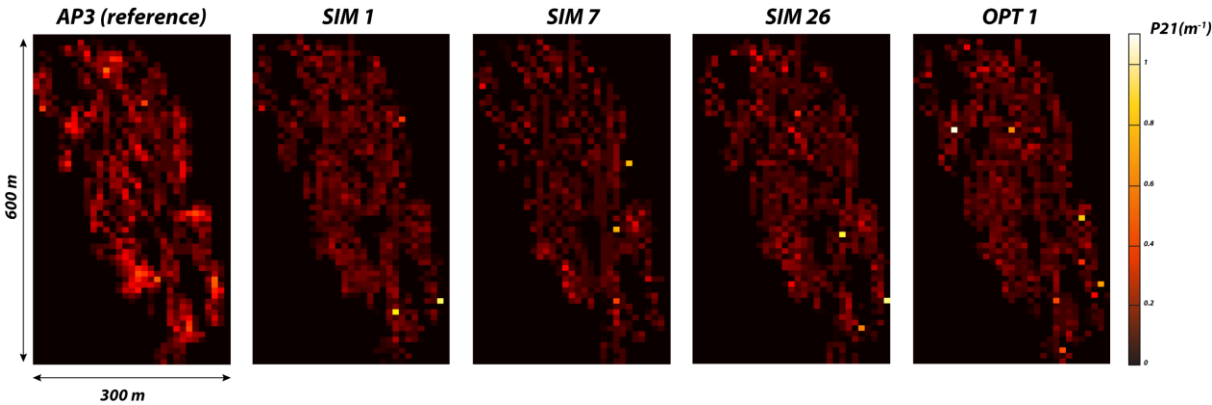
858 **Figure 11:** A) Partitioning of AP4 in 3 EZ. B) probability map and associated statistics for

859 each EZ. C) training images associated with the partition of AP4. D) hard conditioning data

860 for AP4
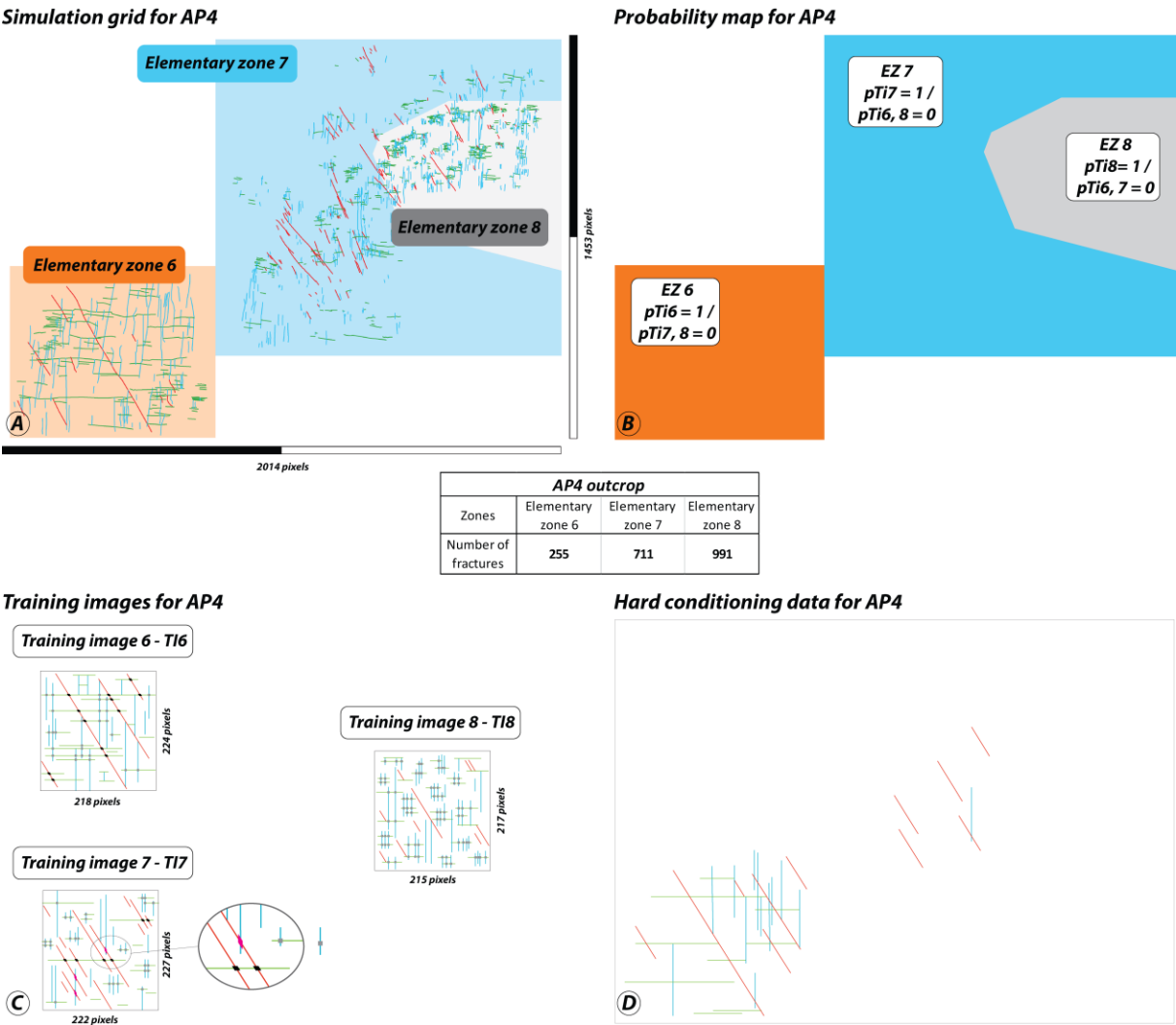
870 **Figure 12:** Comparison of the AP4 original outcrop with a MPS simulated version AP4-1

871

872

873

874

875

876

877

878

879

880

881

882

883

884

885

886

887

888

889
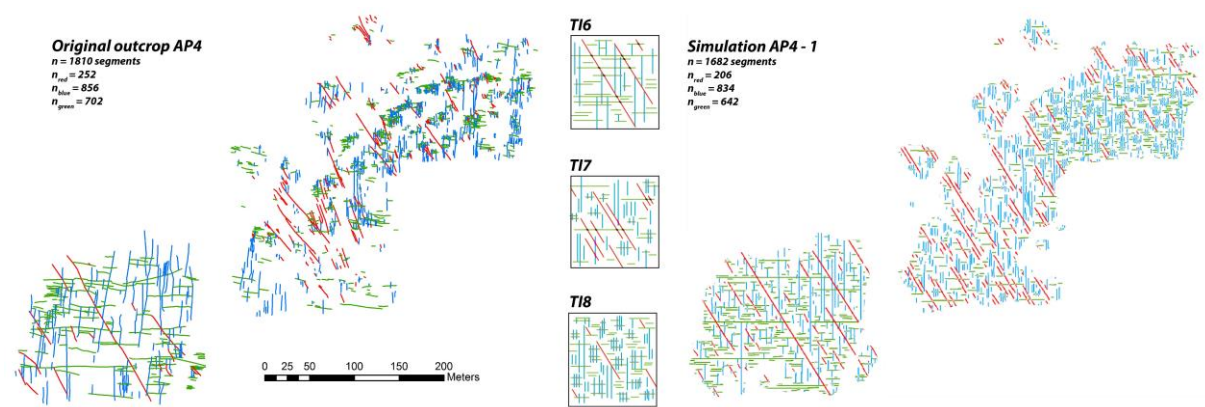
890 **Figure 13:** Smooth probability map at the reservoir scale (combination of AP3 and AP4). A)

891 Relative position of AP3 and AP4 outcrops. B) Apodi fault added into the area of interest.

892 Extension of the probability map regions in AP3 and AP4 without geological drivers C) and

893 with the influence of the Apodi fault D). Probability maps with smooth transition zones

894 without geological drivers E) and with the influence of the Apodi fault F).

895

896

897

898
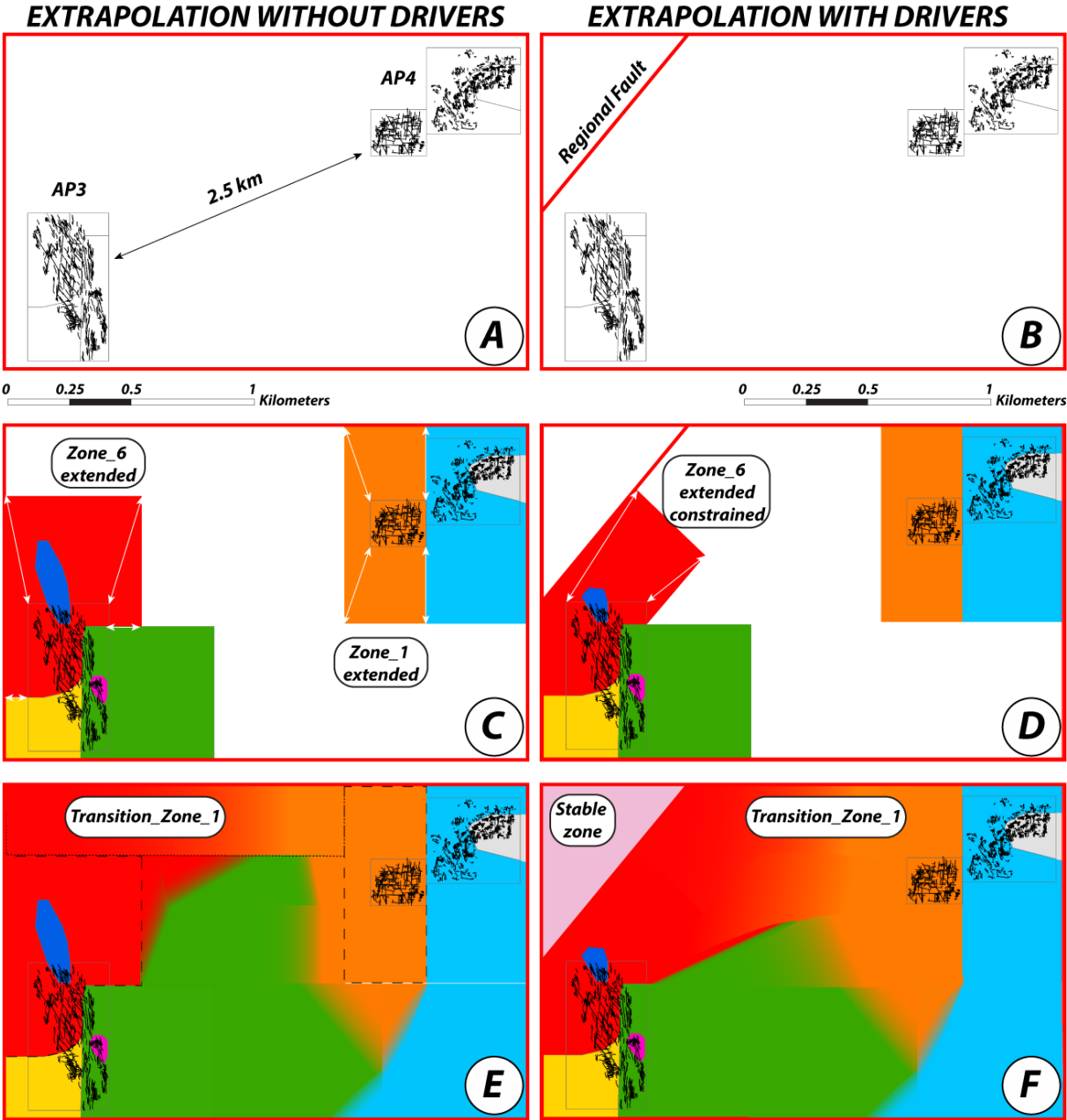
899 **Figure 14:** Fracture network extrusion in 3D. The method consists of identifying the different

900 fracture units (FU) on which the fracture height is supposed to be constant (A). This method

901 requires one simulation per top fracture unit (SIM SLICES). (B) is a 3D DFN based on the

902 hypothetical case (A) and realised in gOcad software. (C) is a cross section realised in the

903 centre of the 3D model in the E-W direction.

904
905
906
907
908
909
910
911
912
913
914
915
916
917
918
919
920
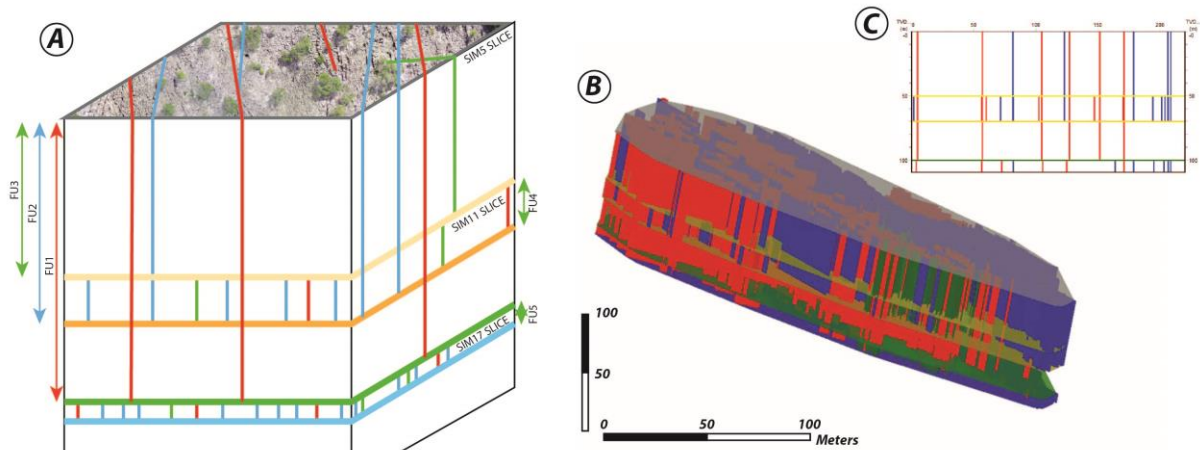
References

Agar, S. M. and Geiger, S.: Fundamental controls on fluid flow in carbonates: current workflows to emerging technologies, Geological Society, London, Special Publications, 406, 60, 2015.

Angelim, L. A. A., Medeiros, V. C., and Nesi, J. R.: Mapa geológico do Estado do Rio Grande do Norte, CPRM/FAPERN, Recife, Projeto Geologia e Recursos Minerais do Estado do Rio Grande do Norte, 2006.

Bemis, S. P., Micklethwaite, S., Turner, D., James, M. R., Akciz, S., Thiele, S. T., and Bangash, H. A.: Ground-based and UAV-Based photogrammetry: A multi-scale, high-resolution mapping tool for structural geology and paleoseismology, Journal of Structural Geology, 69, 163-178, 2014.

Berkowitz, B.: Characterizing flow and transport in fractured geological media: A review, Advances in Water Resources, 25, 861-884, 2002.

Bertotti, G., de Graaf, S., Bisdom, K., Oskam, B., Vonhof, H. B., Bezerra, F. H. R., Reijmer, J. J. G., and Cazarin, C. L.: Fracturing and fluid-flow during post-rift subsidence in carbonates of the Jandaira Formation,Potiguar Basin,NE Brazil, Basin Research, 29, 18, 2017.

Bisdom, K.: Burial-related fracturing in sub-horizontal and folded reservoirs - Geometry, geomechanics and impact on permeability, Doctorate, Technische Universiteit Delft, 2016.

Bisdom, K., Gauthier, B. D. M., Bertotti, G., and Hardebol, N. J.: Calibrating discrete fracture-network models with a carbonate three-dimensional outcrop fracture network: Implications for naturally fractured reservoir modeling, AAPG Bulletin, 98, 1351-1376, 2014.

Bisdom, K., Nick, H. M., and Bertotti, G.: An integrated workflow for stress and flow modelling using outcrop-derived discrete fracture networks, Computers & Geosciences, 103, 21-35, 2017.

Bruna, P.-O., Guglielmi, Y., Viseur, S., Lamarche, J., and Bildstein, O.: Coupling fracture facies with in-situ permeability measurements to generate stochastic simulations of tight carbonate aquifer properties: Example from the Lower Cretaceous aquifer, Northern Provence, SE France, Journal of Hydrology, 529, Part 3, 737-753, 2015.

Bruna, P.-O., Hardebol, N., Bisdom, K., Straubhaar, J., Mariethoz, G., and Bertotti, G.: 2D to 3D fracture network detection and forecasting in a carbonate reservoir analogue using Multiple Point Statistics (MPS). ExCEL London2017.

Bruna, P.-O., Prabhakaran, R., Bertotti, G., Mittempergher, S., Succo, A., Bistacchi, A., Storti, F., and Meda, M.: Multiscale 3D prediction of fracture network geometry and fluid flow efficiency in folded carbonate reservoir analogues; Case study of the Island of Pag (Croatia). Muscat, Oman, 5-7 February 2018 2018.

Chopra, S. and Marfurt, K. J.: Volumetric curvature attributes for fault/fracture characterization, First Break, 25, 12, 2007.

Chugunova, T., Corpel, V., and Gomez, J.-P.: Explicit fracture network modelling: from multiple point statistics to dynamic simulation, Mathematical Geosciences, 49, 13, 2017.

Claes, H., Degros, M., Soete, J., Claes, S., Kele, S., Mindszenty, A., Török, Á., El Desouky, H., Vanhaecke, F., and Swennen, R.: Geobody architecture, genesis and petrophysical characteristics of the Budakalász travertines, Buda Hills (Hungary), Quaternary International, 437, 107-128, 2017.

Corradetti, A., Tavani, S., Parente, M., Iannace, A., Vinci, F., Pirmez, C., Torrieri, S., Giorgioni, M., Pignalosa, A., and Mazzoli, S.: Distribution and arrest of vertical through-going joints in a seismic-scale carbonate platform exposure (Sorrento peninsula, Italy): insights from

967   integrating field survey and digital outcrop model, Journal of Structural Geology, doi:
968   https://doi.org/10.1016/j.jsg.2017.09.009, 2017a. 2017a.
969   Corradetti, A., Tavani, S., Russo, m., Arbues, P. C., and Granado, P.: Quantitative analysisi of
970   folds by means of orthorectified photogrammetric 3D models: A case study from Mt. Catria,
971   Northern Apennines, Italy, The photogrammetric record, doi: 10.1111/phor.12212, 2017b.
972   17, 2017b.
973   Costa de Melo, A. C., de Castro, D. L., Bezerra, F. H. R., and Bertotti, G.: Rift fault geometry
974   and evolution in the Cretaceous Potiguar Basin (NE Brazil) based on fault growth models,
975   Journal of South American Earth Sciences, 71, 96-107, 2016.
976   Council, N. R.: Rock Fractures and Fluid Flow: Contemporary Understanding and
977   Applications, The National Academies Press, Washington, DC, 1996.
978   de Brito Neves, B. B., Fuck, R. A., Cordani, U. G., and Thomaz F°, A.: Influence of basement
979   structures on the evolution of the major sedimentary basins of Brazil: A case of tectonic
980   heritage, Journal of Geodynamics, 1, 495-510, 1984.
981   Dershowitz, W. S. and Herda, H.: Interpretation of Fracture Spacing and Intensity,
982   Balkema1992.
983   Deutsch, C. V. and Journel, A. G.: GSLIB : Geostatistical software library and user's guide,
984   New York, 1997.
985   Gringarten, E. and Deutsch, C. V.: Methodology for Variogram Interpretation and Modeling
986   for Improved Reservoir Characterization, SPE Annual Technical Conference and Exhibition,
987   Texas, Houston, 1999.
988   Gringarten, E. and Deutsch, C. V.: Teacher's Aide Variogram Interpretation and modeling,
989   Mathematical Geology, 33, 507-534, 2001.
990   Hanke, J. R., Fischer, M. P., and Pollyea, R. M.: Directional semivariogram analysis to identify
991   and rank controls on the spatial variability of fracture networks, Journal of Structural
992   Geology, 108, 34-51, 2018.
993   Hooker, J. N., Laubach, S. E., and Marrett, R.: Fracture-aperture size—frequency, spatial
994   distribution, and growth processes in strata-bounded and non-strata-bounded fractures,
995   Cambrian Mesón Group, NW Argentina, Journal of Structural Geology, 54, 54-71, 2013.
996   Huang, N., Jiang, Y., Liu, R., and Li, B.: Estimation of permeability of 3-D discrete fracture
997   networks: An alternative possibility based on trace map analysis, Engineering Geology, 226,
998   12-19, 2017.
999   Journel, A. and Zhang, T.: The Necessity of a Multiple-Point Prior Model, Mathematical
1000 Geology, 38, 591-610, 2006.
1001 Journel, A. G.: Beyond Covariance: The Advent of Multiple-Point Geostatistics. In:
1002 Geostatistics Banff 2004, Leuangthong, O. and Deutsch, C. V. (Eds.), Springer Netherlands,
1003 Dordrecht, 2005.
1004 Jung, A., Fenwick, D. H., and Caers, J.: Training image-based scenario modeling of fractured
1005 reservoirs for flow uncertainty quantification, Computational Geosciences, 17, 1015-1031,
1006 2013.
1007 Karimpouli, S., Tahmasebi, P., Ramandi, H. L., Mostaghimi, P., and Saadatfar, M.: Stochastic
1008 modeling of coal fracture network by direct use of micro-computed tomography images,
1009 International Journal of Coal Geology, 179, 153-163, 2017.
1010 Kovesi, P.: MATLAB and Octave Functions for Computer Vision and Image Processing. 2000.
1011 Lamarche, J., Chabani, A., and Gauthier, B. D. M.: Dimensional threshold for fracture linkage
1012 and hooking, Journal of Structural Geology, doi: https://doi.org/10.1016/j.jsg.2017.11.016,
1013 2017. 2017.

1014 Lamarche, J., Lavenu, A. P. C., Gauthier, B. D. M., Guglielmi, Y., and Jayet, O.: Relationships
1015 between fracture patterns, geodynamics and mechanical stratigraphy in Carbonates (South-
1016 East Basin, France), Tectonophysics, 581, 231–245, 2012.
1017 Laubach, S. E., Lamarche, J., Gauthier, B. D. M., Dunne, W. M., and Sanderson, D. J.: Spatial
1018 arrangement of faults and opening-mode fractures, Journal of Structural Geology, 108, 2-15,
1019 2018.
1020 Laubach, S. E., Olson, J. E., and Gross, M. R.: Mechanical and fracture stratigraphy, AAPG
1021 Bulletin, 93, 1413–1426, 2009.
1022 Lavenu, A. P. C., Lamarche, J., Gallois, A., and Gauthier, B. D. M.: Tectonic versus diagenetic
1023 origin of fractures in a naturally fractured carbonate reservoir analog (Nerthe anticline,
1024 southeastern France), AAPG Bulletin, 97, 2207-2232, 2013.
1025 Li, J. Z., Laubach, S. E., Gale, J. F. W., and Marrett, R. A.: Quantifying opening-mode fracture
1026 spatial organization in horizontal wellbore image logs, core and outcrop: Application to
1027 Upper Cretaceous Frontier Formation tight gas sandstones, USA, Journal of Structural
1028 Geology, 108, 137-156, 2018.
1029 Liu, X., Srinivasan, S., and Wong, D.: Geological characterization of naturally fractured
1030 reservoirs using multiple point geostatistics, 2002.
1031 Liu, X., Zhang, C., Liu, Q., and Birkholzer, J.: Multiple-point statistical prediction on fracture
1032 networks at Yucca Mountain, Environmental Geology, 57, 1361-1370, 2009.
1033 Lloyd, S. P.: Least Squares Quantization in PCM, IEEE Transactions on Information Theory, 28,
1034 9, 1982.
1035 Long, J. C. S. and Witherspoon, P. A.: The relationship of the degree of interconnection to
1036 permeability in fracture networks, Journal of Geophysical Research, 90, 12, 1985.
1037 Magistroni, C., Meda, M., and Corrao, A.: Faults and fracture network prediction:
1038 stress/strain modelling from outcrop analysis to seismic characterisation, Abu Dhabi, UAE,
1039 10-13 November 2014 2014.
1040 Mariethoz, G.: Geological stochastic imaging for aquifer characterization, Doctorate, Faculté
1041 des Sciences, Université de Neuchâtel, 229 pp., 2009.
1042 Mariethoz, G., Renard, P., and Straubhaar, J.: The Direct Sampling method to perform
1043 multiplepoint geostatistical simulations., Water Resources research, 46, 2010.
1044 Marrett, R., Gale, J. F. W., Gómez, L. A., and Laubach, S. E.: Correlation analysis of fracture
1045 arrangement in space, Journal of Structural Geology, 108, 16-33, 2018.
1046 Mauldon, M., Dunne, W. M., and Rohrbaugh, M. B. J.: Circular scanlines and circular
1047 windows: new tools for characterizing the geometry of fracture traces. , Journal of Structural
1048 Geology, 23, 12, 2001.
1049 Meerschman, E., Pirot, G., Mariethoz, G., Straubhaar, J., Van Meirvenne, M., and Renard, P.:
1050 A practical guide to performing multiple-point statistical simulations with the Direct
1051 Sampling algorithm, Computers & Geosciences, 52, 307-324, 2013.
1052 Montanari, D., Minissale, A., Doveri, M., Gola, G., Trumpy, E., Santilano, A., and Manzella, A.:
1053 Geothermal resources within carbonate reservoirs in western Sicily (Italy): A review, Earth-
1054 Science Reviews, 169, 180-201, 2017.
1055 Olson, J. E., Laubach, S. E., and Lander, R. H.: Natural fracture characterization in tight gas
1056 sandstones: Integrating mechanics and diagenesis, AAPG Bulletin, 93, 1535-1549, 2009.
1057 Oriani, F., Ohana-Levi, N., Marra, F., Straubhaar, J., Mariethoz, G., Renard, P., Karnieli, A.,
1058 and Morin, E.: Simulating Small-Scale Rainfall Fields Conditioned by Weather State and
1059 Elevation: A Data-Driven Approach Based on Rainfall Radar Images, Water Resources
1060 Research, 53, 8512-8532, 2017.

Otsu, N.: A Threshold Selection Method from Gray-Level Histograms, IEEE Transactions on Systems, Man, and Cybernetics, 9, 5, 1979.

Panza, E., Sessa, E., Agosta, F., and Giorgioni, M.: Discrete Fracture Network modelling of a hydrocarbon-bearing, oblique-slip fault zone: Inferences on fault-controlled fluid storage and migration properties of carbonate fault damage zones, Marine and Petroleum Geology, 89, Part 2, 263-279, 2018.

Reis, Á. F. C., Bezerra, F. H. R., Ferreira, J. M., do Nascimento, A. F., and Lima, C. C.: Stress magnitude and orientation in the Potiguar Basin, Brazil: Implications on faulting style and reactivation, Journal of Geophysical Research: Solid Earth, 118, 5550-5563, 2013.

Rzonca, B.: Carbonate aquifers with hydraulically non-active matrix: A case study from Poland, Journal of Hydrology, 355, 202-213, 2008.

Solano, N., Zambrano, L., and Aguilera, R.: Cumulative Gas Production Distribution on the Nikanassin Tight Gas Formation, Alberta and British Columbia, Canada, Trinidad and Tobago Energy Resources Conference, Port of Spain, Trinidad, 26, 2010.

Somasundaram, S., Mund, B., Soni, R., and Sharda, R.: Seismic attribute analysis for fracture detection and porosity prediction: A case study from tight volcanic reservoirs, Barmer Basin, India, The Leading Edge, 36, 7, 2017.

Straubhaar, J.: Deesse user's guide. The Centre for Hydrogeology and Geothermics (CHYN), U. o. N. (Ed.), Neuchâtel, Switzerland, 2017.

Straubhaar, J., Renard, P., Mariethoz, G., Froidevaux, R., and Besson, O.: An improved parallel multiple-point algorithm using a list approach., Mathematical Geosciences, 43, 24, 2011.

Strebelle, S.: Conditional Simulation of Complex Geological Structures Using Multiple-Point Statistics, Mathematical Geology, 34, 1-21, 2002.

Tavani, S., Corradetti, A., and Billi, A.: High precision analysis of an embryonic extensional fault-related fold using 3D orthorectified virtual outcrops: The viewpoint importance in structural geology, Journal of Structural Geology, 86, 200-210, 2016.

Van Eijk, M.: Analysis of the fracture network in carbonate rocks of the Jandaira Formation in northeast Brazil, 2014. Technische Universiteit Delft, 60 pp., 2014.

Vollgger, S. A. and Cruden, A. R.: Mapping folds and fractures in basement and cover rocks using UAV photogrammetry, Cape Liptrap and Cape Paterson, Victoria, Australia, Journal of Structural Geology, 85, 168-187, 2016.

Wang, S., Huang, Z., Wu, Y.-S., Winterfeld, P. H., and Zerpa, L. E.: A semi-analytical correlation of thermal-hydraulic-mechanical behavior of fractures and its application to modeling reservoir scale cold water injection problems in enhanced geothermal reservoirs, Geothermics, 64, 81-95, 2016.

Wu, J., Boucher, A., and Zhang, T.: A SGeMS code for pattern simulation of continuous and categorical variables: FILTERSIM, Computers & Geosciences, 34, 1863-1876, 2008.

Zhang, L., Kang, Q., Chen, L., Yao, J.: Simulation of flow in multi-scale porous media using the lattice boltzmann method on quadtree grids, Communications in Computational Physics 19, 17, 2016.